Published in final edited form as:

Neuron. 2020 August 05; 107(3): 522–537.e6. doi:10.1016/j.neuron.2020.04.025.

Rapid 3D Enhanced Resolution Microscopy Reveals Diversity in Dendritic Spinule Dynamics, Regulation, and Function

Colleen R. Zaccard[1], **Lauren Shapiro**[1], **Maria D. Martin-de-Saavedra**[1], **Christopher Pratt**[1], **Kristoffer Myczek**[1], **Amy Song**[1], **Marc P. Forrest**[1], **Peter Penzes**[1,2,3,*]

[1]Department of Physiology, Northwestern University, Chicago, IL 60611, USA

[2]Department of Psychiatry and Behavioral Sciences, Northwestern University, Chicago, IL 60611, USA

[3]Lead Contact

SUMMARY

Dendritic spinules are thin protrusions, formed by neuronal spines, not adequately resolved by diffraction-limited light microscopy, which has limited our understanding of their behavior. Here we performed rapid structured illumination microscopy and enhanced resolution confocal microscopy to study spatiotemporal spinule dynamics in cortical pyramidal neurons. Spinules recurred at the same locations on mushroom spine heads. Most were short-lived, dynamic, exploratory, and originated near simple PSDs, whereas a subset was long-lived, elongated, and associated with complex PSDs. These subtypes were differentially regulated by Ca^{2+} transients. Furthermore, the postsynaptic Rac1-GEF kalirin-7 regulated spinule formation, elongation, and recurrence. Long-lived spinules often contained PSD fragments, contacted distal presynaptic terminals, and formed secondary synapses. NMDAR activation increased spinule number, length, and contact with distal presynaptic elements. Spinule subsets, dynamics, and recurrence were validated in cortical neurons of acute brain slices. Thus, we identified unique properties, regulatory mechanisms, and functions of spinule subtypes, supporting roles in neuronal connectivity.

In Brief

Enhanced resolution 3D microscopy reveals the dynamics of thin dendritic spine protrusions, termed spinules, which are uniquely regulated by local Ca^{2+} and the Rac1-GEF kalirin-7. The majority are small, short-lived, dynamic, and recurrent, whereas an elongated subset is activity-induced, stabilized by distal presynaptic terminals, and can form connectivity-altering secondary synapses.

*Correspondence: p-penzes@northwestern.edu.

AUTHOR CONTRIBUTIONS

Project supervision, P.P.; Conceptualization and Manuscript Preparation, C.R.Z. and P.P.; Method Validation, Data Collection, and Analysis, C.R.Z., L.S., M.D.M.-d.-S., C.P., A.S., M.P.F., and K.M.

SUPPLEMENTAL INFORMATION

Supplemental Information can be found online at https://doi.org/10.1016/j.neuron.2020.04.025.

DECLARATION OF INTERESTS

The authors declare no competing interests.

Graphical Abstract

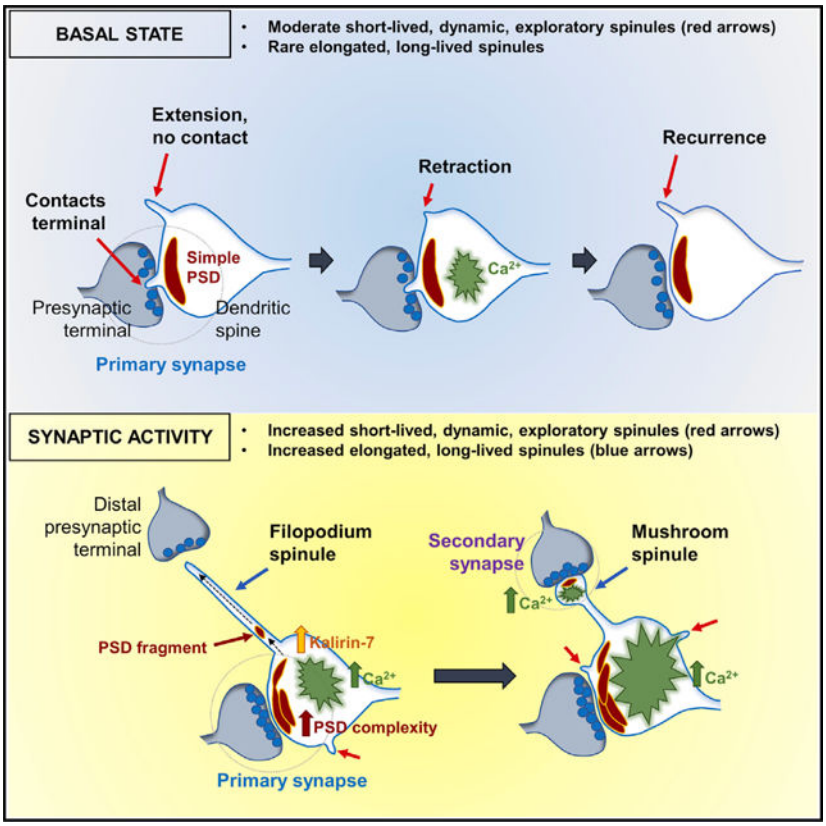

INTRODUCTION

Dendritic spinules, first detected in hippocampal neurons using electron microscopy (EM) (Westrum and Blackstad, 1962; Tarrant and Routtenberg, 1977), are thinner than filopodia, typically less than 1 μm in length, often detected on large mushroom spines, and inducible by synaptic activity (Petralia et al., 2015). An EM study of the mature rat hippocampus reported that 91% of mushroom and 24% of thin spines had 1 or more spinules in the basal state (Spacek and Harris, 2004), suggesting their common occurrence in healthy native brain tissue. These nanoscale structures cannot be adequately resolved by diffraction-limited light microscopy. Therefore, our understanding of spinule structure and function has largely been inferred from fixed tissue EM (Tao-Cheng et al., 2009; Spacek and Harris, 2004) and a few limited-resolution confocal and two-photon imaging studies (Richards et al., 2005; Ueda and Hayashi, 2013). Some EM studies have reported spinule origination from perforations or edges of complex postsynaptic densities (PSDs) (Toni et al., 2001; Dhanrajan et al., 2004; Spacek and Harris, 2004), whereas others have described their emergence from non-perforated PSD edges or spine necks (Sorra et al., 1998; Tao-Cheng et al., 2009). Consequently, the dynamic relationship between spinule formation and PSD remodeling remains to be clarified.

Spinules can be induced by neuronal depolarization and N-methyl-D-aspartate (NMDA) treatment (Tao-Cheng et al., 2009) as well as theta burst stimulation and glutamate application (Ueda and Hayashi, 2013). Although studies show that Ca^{2+}, a key signaling ion in synaptic transmission, regulates spinule-dependent synaptic plasticity in fish horizontal cells (Country and Jonz, 2017), the role of Ca^{2+} in mammalian spinule regulation remains unclear. Actin regulatory pathways may be involved in spinule development (Colicos et al., 2001), and PIP_3 has been shown to regulate spinules during structural long-term potentiation (sLTP) (Ueda and Hayashi, 2013). One study noted F-actin-driven spinules induced by electrical stimulation (Colicos et al., 2001), whereas another described "spine head protrusions" driven by Rac1-dependent elongation of F-actin barbed ends away from the PSD (Chazeau et al., 2014). We investigated the roles of the local Ca^{2+} and actin regulator kalirin-7, which could modulate spinules downstream of PIP_3 and Ca^{2+} signals, in mammalian spinule formation.

Spinules can project into presynaptic boutons, potentially mediating postsynaptic membrane remodeling and retrograde signaling via *trans*-endocytosis (Spacek and Harris, 2004; Petralia et al., 2015). One study has reported outgrowth of thin membrane protrusions toward new presynaptic actin puncta, suggesting a role in synapse formation (Colicos et al., 2001). However, past studies have relied on EM of fixed tissues or diffraction-limited live microscopy. Super-resolution imaging modalities have enabled live imaging of nanoscale structures (Cox, 2015; Godin et al., 2014), but their early application for volumetric samples was limited. Stimulated emission depletion (STED) was applied to study spine remodeling in response to chemical long-term potentiation (cLTP) and holographic photo-stimulation (Nägerl et al., 2008; Lauterbach et al., 2016). Structured illumination microscopy (SIM) is well suited for live 3D imaging (Fiolka et al., 2012), and custom modifications have improved acquisition speed (Kner et al., 2009; Li et al., 2015). Here we employed rapid SIM and enhanced resolution confocal microscopy, where 3D deconvolution afforded ~1.5 times resolution improvement (Holmes and Liu, 1989; Biggs, 2010), to visualize spinules and investigate their behavior, regulatory mechanisms, and function.

Our study demonstrates a new application of rapid SIM and enhanced resolution confocal microscopy to investigate sub-spine structures, revealing spinule subsets divergent in shape, dynamics, regulation, and function. We also show positive spinule regulation by Ca^{2+} and kalirin-7. Morphological subtypes differ in local Ca^{2+} transients and their ability to traffic PSD fragments and contact distal synapses. Activity-induced elongated spinules extend to preferentially contact spine head distal presynaptic terminals, suggesting a role in "multi-contact synapse" formation. Finally, we validated our main findings in acute mouse brain slices, providing the impetus for studies of the role of spinules in synaptic plasticity and neuropsychiatric diseases.

RESULTS

Rapid Time-Lapse SIM Reveals Spinule Recurrence and Divergent Lifespans

To examine the spatiotemporal dynamics of spinules, we first utilized a SIM system with improved optical sectioning speed for live imaging of dissociated cortical mouse pyramidal neurons expressing dsRedExpress2. We balanced acquisition speed against photobleaching

and phototoxicity to resolve dynamic, thin protrusions that were finer than filopodia and originated from dendritic spines (i.e., spinules) at 15- to 20-s z-intervals. Similar to a previous study (Spacek and Harris, 2004), Imaris 3D reconstructions revealed spinules on mushroom, branched, and, rarely, thin spines (Figure 1A). Mushroom spines displayed the highest mean number of spinules over the 1,000-s imaging duration (Figure 1B). We observed that 85% of mushroom spines were spinule(+) over time, whereas 15% were spinule(−) (Figure 1C). To show that spinule formation was not a byproduct of excessive photo-stimulation, we compared spinule number per spine in the first five to the last five z stacks and found no difference (Figure S1A). We next tracked mushroom spine volume over time (Figure 1D), revealing a strong positive correlation between spinule number and mean spine head volume (Figure 1E). Spinules were often observed in non-contiguous z stacks at the same topographical spine head locations, repeatedly extending and retracting along nearby axons (Figure 1F; Video S1). We quantified normalized spinule origination in relation to kymograph outlines of spine heads (Figure 1G) to show that recurring spinules were more frequent than singly occurring spinules per spine over 1,000 s and that spinules could recur up to six times at one location (Figure 1H). Most spinules (70%) existed for less than 60 s, whereas fewer existed for 60 s or more, in rare cases exceeding the imaging duration (Figures 1I and S1B). Accordingly, short-lived spinules were more frequent per spine (Figure 1J). A representative spine displayed multiple short-lived tapered or vermiform spinules and fewer long-lived spinules (Figures 1K, S1C, and S1D). Long-lived spinules displayed diverse spine-like morphologies (e.g., filopodia and mushroom) and occasionally originated from spine necks or trafficked presumptive vesicles within thick spinules (Figures 1L and S1E).

Short- and Long-Lived Spinules Differ in Dimensions and Dynamics

Mean spinule length (0.49 μm) and volume positively correlated with lifespan (Figures 2A and S2A–S2E). A comparison of mean and maximum spinule length grouped according to lifespan revealed no significant difference between the less than 20 s and the 20 or more but less than 60 s groups, whereas both differed from the 60 s or more group (Figure S2F). Hence, we designated two spinule subgroups for further comparison, short-lived (<60 s) and long-lived (≥60 s). Long-lived spinules were greater in mean and maximum length (Figure 2B), with no difference in width between the two groups (Figure S2G). We tracked spinule volumes in Imaris to generate temporal spinule volume plots (Figure 2C) and illustrate the differential size and stability of short-versus long-lived spinules (Figures 2D and 2E). Overall, mean and maximum volume were greater in long-lived spinules (Figure 2F). We found a negative correlation between spinule length change per second and lifespan (Figure 2G). Although cumulative length and volume change were greatest in long-lived spinules (Figures S2H and S2I), changes in length and volume per second were heightened in short-lived spinules (Figures 2H and 2I).

Spinule Subtypes Have Distinct Relationships with the PSD

To investigate the dynamic relationship between spinules and the PSD, we utilized plasmid-encoded mRuby as a cell fill and GFP-tagged “intrabodies” to label endogenous PSD95 (Gross et al., 2013), followed by enhanced resolution confocal microscopy to mitigate intrabody photobleaching observed with SIM (Figure 3A). The majority (91%) of

mushroom spines detected were spinule(+) over 600 s of imaging (Figure S3A). We again observed rare elongated, long-lived spinules and frequent short-lived spinules, and the shorter z-interval of ~8 s enabled detection of a third “lightning” spinule subgroup (<20 s) (Figures S3B and S3C). Again, spinule length positively correlated with lifespan, and length was greater in long-versus short-lived spinules (Figures S3D and S3E). Short-lived spinules typically originated near the PSD edge (Figure 3B), whereas long-lived spinules originated further from complex PSDs (Figure 3C). The mean distance from the spinule base to the PSD edge was significantly lesser in short-lived (0.28 μm) versus long-lived spinules (0.43 μm) (Figures 3D and 3E). PSD volume and dynamics did not correlate with spinule number per spine (Figures 3F, 3G, S3F, and S3G). Strikingly, 78% of spines forming long-lived spinules displayed complex, partitioned PSDs compared with 23% of long-lived spinule(−) spines (Figure 3H), and 67% of long-lived spinule(+) spines displayed fragmented PSDs versus 28% of long-lived spinule(−) spines (Figure 3I). Mean and maximum PSD fragment numbers per stack were significantly greater in long-lived(+) compared with long-lived spinule(−) spines (Figure 3J). We observed PSD fragments repeatedly entering a long-lived spinule (Figure 3K) and a fragment trafficking in and out of a filopodium spinule tip (Figure 3L; Video S2). Although we never observed PSD fragments in short-lived spinules, 25% of long-lived spinules contained a PSD fragment at one or more z-intervals (Figure 3M).

Spinule Morphological Subtypes Are Differentially Regulated by Calcium

Neuronal activity has been shown to induce spinule formation (Ueda and Hayashi, 2013; Petralia et al., 2015), but the role of Ca^{2+} in mammalian spinule formation had not been examined. We utilized fast (~2 s/z stack) enhanced resolution confocal imaging of neurons expressing mRuby and the Ca^{2+} sensor GCaMP6s (Chen et al., 2013). Interestingly, we visualized isolated Ca^{2+} nanodomains appearing in long-lived spinules during periodic spine head Ca^{2+} transients (Figures 4A and S4A). Plots of GCaMP6 mean fluorescence intensity (MFI) over time revealed synchrony of Ca^{2+} transients between spinules and corresponding spine heads and dendritic shafts (Figures 4B and S4B).

To evaluate the requirement for intracellular Ca^{2+} in spinule formation, we compared vehicle-treated control neurons with those treated with the cell-permeant Ca^{2+} chelator BAPTA-AM. Spinule number and cumulative spinule lifespan per spine were significantly higher in controls than in BAPTA-AM-treated neurons (Figures 4C and 4D). Control mushroom spines frequently formed short- and long-lived spinules (Figure 4E; Video S3), whereas BAPTA-AM-treated spines formed fewer spinules (Figure 4F). As shown by the normalized change in Ca^{2+} fluorescence ($\Delta F/F_0$) and corresponding spatiotemporal spinule maps, spines with frequent high-amplitude Ca^{2+} transients displayed many short-lived and fewer long-lived spinules (Figure 4G), whereas spines with sporadic peaks formed only short-lived spinules (Figures S4C and S4D). In contrast, spines from BAPTA-AM-treated neurons displayed greatly dampened Ca^{2+} transients and fewer spinules (Figure 4H). Assessment of Ca^{2+} peaks in spines (i.e., a 50% increase in $\Delta F/F_0$ above baseline) revealed a positive correlation between total spinule number per spine and peak amplitude (Figure S4E) but no correlation with peak frequency or duration. Interestingly, short-lived spinule number per spine positively correlated with Ca^{2+} peak mean and maxima (Figure 4I), whereas long-lived spinule number positively correlated with Ca^{2+} peak frequency and duration. Tracking

GCaMP6 MFI in short- and long-lived spinules on the same spine revealed short-lived and filopodia-like spinules with lower transients compared with mushroom spinules, which displayed distinctive and often staggered Ca^{2+} transient patterns (Figures 4J, 4K, and S4F; Video S4). A comparison of co-existing long- and short-lived spinules revealed heightened Ca^{2+} transients in long-lived spinules during periods of inactivity and activity in spine heads (Figure 4L).

The Rac1-GEF Kalirin-7 Promotes Spinule Dynamics

We next investigated a candidate protein that could regulate spinules via the actin dynamics regulatory pathway, downstream of PIP_3 and Ca^{2+} signals. Kalirin is a guanine nucleotide exchange factor (GEF) with a central role in spine structural plasticity downstream of NMDA receptors (NMDARs), inducing Ca^{2+}/calmodulin-dependent protein kinase II (CaMKII)-dependent-activation of the Rho-GTPase Rac-1 to promote actin polymerization and spine head enlargement (Xie et al., 2007). Kalirin's Sec14p-like domain, encompassing the CaMKII phosphorylation site, binds to PIP_3 (Miller et al., 2015). Kalirin regulates spine maturation and maintenance, postsynaptic actin dynamics, and activity-dependent plasticity and is important for learning and memory (Ma et al., 2001; Xie et al., 2007). Kalirin-7, the most common isoform in the adult brain, is highly enriched at the PSD. Hence, we investigated the role of kalirin-7 in spinule dynamics. We expressed exogenous kalirin-7 or control plasmids in cortical neurons, followed by live enhanced resolution confocal imaging (Figures 5A and S5A; Videos S5 and S6). We observed an abundance of spinules on kalirin-7-expressing mushroom spines over 5 min that often displayed long filopodia-like morphologies (Figure 5B), whereas control spines displayed fewer small spinules with tapered or vermiform shapes (Figure 5C). Exogenous kalirin-7 expression increased total linear spine density and volume compared with controls (Figures S5B–S5E). Spinule number per mushroom spine was significantly higher in kalirin-7-expressing neurons than in controls when normalized to spine volume (Figures 5D and S5F), indicating that the effect was not a result of increased spine size. We observed no significant difference in spinule lifespan or frequency distributions in kalirin-7-expressing neurons versus controls (Figures 5E, S5G, and S5H). Mean and maximum spinule length in kalirin-7-expressing neurons were higher than in controls, with a distribution toward longer spinules (Figures 5F, 5G, S5I, and S5J). The proportion of spinules recurring at the same spine head locations was higher in kalirin-7 neurons versus controls (Figure 5H). Moreover, kalirin-7-induced spinules often repeatedly extended to contact sparsely labeled axons (Figure 5I).

Kalirin-7 Is Required for Normal Spinule Dynamics

When neurons expressed a kalirin-7-targeted short hairpin RNA (shRNA) tagged with GFP and mRuby cell-filling protein for 3 days, mushroom spine volume was significantly reduced compared with the scramble (Figures 6A and S6A–S6D). Spinule number per mushroom spine, normalized to spine volume, was substantially lower in the knockdown (Figures 6B and S6E), and spinule lifespan was also decreased (Figure 6C). Relative and binned frequency distributions showed that most spinules persisted for 30 s or less in the kalirin-7 knockdown (Figures 6D and S6F). Maximum spinule length was also lower in the knockdown (Figure 6E). Importantly, we observed a decline in spinule recurrence at the

same topographical locations in knock-down spines (Figure 6F) and an increase in short- compared with long-lived spinules (Figure 6G).

Spinule Subtypes Form Distinct Presynaptic Contacts

To investigate how spinule morphology relates to PSD content and presynaptic contacts, we imaged fixed GFP-expressing neurons immunostained for the presynaptic terminal marker VGLUT1 and postsynaptic marker PSD95. Approximately 25% of mushroom spines displayed 1 or more spinules, and spinule number per spine increased with spine area (Figures 7A and 7B). Most spinule(−) and (+) mushroom spines contained PSD95, which colocalized with VGLUT1, suggesting that they formed functional synapses (Figure 7C). Spinule lengths ranged from 0.25 to 1.9 μm (Figures 7D and S7A). Short spinules (<0.5 μm) typically neither contained PSD95 puncta nor directly opposed or colocalized with VGLUT1, suggesting an exploratory role (Figures 7E, 7F, and S7B). Long (≥0.5 μm) filopodia and thin-shaped spinules contained PSD95 puncta or contacted VGLUT1-labeled presynaptic terminals, but not both. Strikingly, 100% of long (≥0.5 μm) mushroom spinules contained PSD95 puncta and opposed presynaptic terminals, and in 83.3% of instances, PSD95 and VGLUT1 colocalized at the enlarged spinule tip, suggesting a functional secondary synapse.

Activation Increases Spinule Number, Length, and Contact with Distal Presynaptic Elements

Because spinules can be induced by glutamate (Richards et al., 2005) and can contact presynaptic terminals (Spacek and Harris, 2004), we activated NMDARs by L-amino-phosphonovalerate (APV) withdrawal (Xie et al., 2007) and examined spinules in relation to bassoon-immunolabeled presynaptic terminals 30 min later. To ascertain that photoactivation did not cause artifactual spinule induction, GFP-expressing neurons were fixed prior to staining and imaging. Both conditions yielded small spinules frequently not in contact with bassoon, and basal state spinules occasionally contacted spine head-proximal bassoon puncta, whereas activation caused a dramatic increase in elongated spinules that contacted spine head-distal bassoon (Figure 7G). Activation increased mushroom spine area and spinule number per spine (Figures 7H, S7C, and S7D). Most spines were proximal bassoon(+) under both conditions, suggesting an existing presynaptic partner (Figure S7E). Among spinule(+) spines, 100% of basal state spines and 95% of activated state spines had a presynaptic partner (Figures S7F and S7G). In the basal state, 19% of spines were spinule(+) compared with 28% upon activation (Figure 7I). Activation dramatically increased spinule length (Figures 7J and S7H), precipitating a shift from spinules less than 1 μm to those 1 μm or more (Figure 7K). The mean number of bassoon contacts per spinule was higher in the activated compared with the basal state (Figure 7L). The distribution of spinule-to-presynaptic contacts also changed (Figures 7M and S7I–S7K). In the basal state, 42% of spinules made no presynaptic contacts, and activation reduced this to 32%. In the basal state, 24% of spinules contacted proximal and 28% contacted distal presynaptic terminals, whereas in the activated state, 8% contacted proximal and 51% contacted distal terminals.

We also examined the number of presynaptic contacts made by spinules grouped by length in basal and activated states. Activation increased not only the number of spinules but also

the proportion of elongated (≥1 μm) versus short (<1 μm) spinules (Figure 7N). The number of bassoon contacts positively correlated with spinule length (Figure S7L), and there was a pronounced increase in bassoon contacts in elongated compared with short spinules upon activation (Figure S7M). Nearly half of the short spinules did not contact presynaptic terminals in the basal or activated state, whereas long spinules preferentially contacted distal presynaptic elements in basal and activated states (Figure S7N). Activity-dependent formation of long spinules increased the number of potential presynaptic contacts by a spine, as shown by calculating the number of bassoon puncta and axons within the spine "reach" versus the spine with additional spinule reach (Figures S7O–S7Q). We again noted distinctive elongated spinule morphologies, including filopodia and intermediate, which often contacted multiple distal bassoon puncta, as well as mushroom spinules (Figure 7O).

Validation of Spinule Subtypes and Behavior in Live Cultures and Acute Brain Slices

To validate prior findings in live neurons, we imaged the spatio-temporal dynamics of spinule subtypes in relation to presynaptic terminals. We labeled functional presynaptic terminals in mRuby-expressing neurons by pulsing with FM 1–43 dye during KCl stimulation, followed by live enhanced resolution confocal imaging. We observed dynamic, recurrent, short-lived spinules that failed to contact active presynaptic terminals, whereas others contacted proximal presynaptic terminals (Figure 8A). We also found examples of stable mushroom spinules sustaining contact with distal presynaptic terminals over the 900-s imaging duration (Figure 8B; Video S7).

Finally, we validated our *in vitro* findings of distinct spinule subtypes and recurrence via enhanced resolution time-lapse confocal imaging of the somatosensory cortex in acute mouse brain slices from 1-month transgenic mice expressing yellow fluorescent protein (YFP) in layer V cortical pyramidal neurons (Thy-1-YFP mice). We observed short- and long-lived recurrent spinules at the same topographical spine head locations in 3D reconstructions (Figure 8C; Video S8). Furthermore, we noted morphological subtypes of long-lived spinules resembling those found in culture, including filopodia-, mushroom-, and intermediate-shaped spinules (Figures 8D–8F; Video S9). The majority of mushroom spines (66%) were spinule(+) over time (Figure 8G). Similar to cultured neurons, mushroom spines typically displayed recurring spinules (Figure 8H), and spines often formed short- and/or long-lived spinules (Figure 8I).

DISCUSSION

Spinules were first reported decades ago in EM studies (Westrum and Blackstad, 1962; Tarrant and Routtenberg, 1977); however, most studies have relied on EM of fixed tissue, which has limited our understanding of their behavior. Here we used enhanced resolution time-lapse imaging to identify unique spinule subtypes divergent in lifespan, dynamics, regulation, and function. We propose a model of spinule form and function where, under basal conditions, short-lived, dynamic, exploratory spinules are prevalent and less frequent, long-lived spinules can mediate contact with proximal and/or distal presynaptic terminals. Neuronal activation increases spinule frequency, lifespan, and length, facilitating their

contact with distal presynaptic terminals and, potentially, their ability to form secondary synapses.

Here we investigated fine mushroom spine-originating protrusions in mature pyramidal neurons, termed spinules. Conversely, filopodia are long thin protrusions emanating from axonal growth cones, dendritic growth cones, or dendritic shafts in developing neurons (Hotulainen and Hoogenraad, 2010). Invagination into the presynaptic terminal has been used to define spinules (Petralia et al., 2018), but these structures can also partially wrap around presynaptic terminals (Pappas and Purpura, 1961). Because various protrusions have been reported throughout animal evolution in multiple regions of the central and peripheral nervous systems, spinules may be members of a family of sub-microscopic cellular projections with a broad role in paracrine intercellular communication (Petralia et al., 2015). Numerous studies have reported spinules in the basal state (Sorra et al., 1998; Spacek and Harris, 2004; Erisir and Dreusicke, 2005; Medvedev et al., 2010), whereas one study found low spinule levels in basal slice cultures, which increased upon high K^+ stimulation or NMDAR activation (Tao-Cheng et al., 2009). Inter-study differences may be dependent on basal activity levels, methodology, animal age, fixation, and/or anesthesia. We used a morphological criterion based on a postsynaptic neuronal cell fill to detect spinules in basal cultures, which increased upon NMDAR activation. Spinules were not a byproduct of excessive photostimulation because similar numbers were observed in early- and late-stage live imaging as well as in fixed preparations. Spinules were abundant in basal-state acute brain slices, indicating that they were not artifacts of dissociated cultures.

Enhanced Resolution Microscopy Reveals Subtype-Specific Spinule Dynamics

Our study underscores the utility of two complementary enhanced resolution techniques for studying dynamic, nanoscale postsynaptic projections in volumetric samples. Although rapid SIM was ideal for distinguishing fine structural details at moderate acquisition speeds, enhanced resolution confocal imaging was optimal for fast multi-channel imaging. Mirroring those seen in slice cultures by EM (Tao-Cheng et al., 2009), we observed diverse spinule morphologies and characterized their distinct properties. Most spinules were short and dynamic, whereas a subset of elongated, long-lived spinules formed filopodia, thin, and mushroom spine-like shapes, echoing spine classes and perhaps indicating divergent functions. Spinules emerged repeatedly from the same topographical spine head locations, often extending and retracting along axons. Spinule recurrence suggests localized molecular machinery at spinule origination sites. Similar to spinules, PSDs continually alter their shape in response to synaptic activity (Okabe et al., 1999; Bourne and Harris, 2008). Some EM studies have reported spinules originating from complex PSD perforations (Toni et al., 2001; Spacek and Harris, 2004; Dhanrajan et al., 2004; Tao-Cheng et al., 2009), whereas another showed their emergence from non-perforated PSD edges or spine necks and contact with distal presynaptic elements (Sorra et al., 1998). Our data showed that short-lived spinules originate near simple PSD edges, whereas long-lived spinules originate farther from complex fragmented PSDs and can traffic PSD fragments.

Mechanisms Regulating Spinule Dynamics

NMDAR activation promoted spinule formation, growth, and elongation and their contact with distal presynaptic terminals. These findings are consistent with previous reports of their induction by various types of stimulation; i.e., estradiol (Murphy and Andrews, 2000), high K^+ depolarization (Tao-Cheng et al., 2009), cLTP (Stewart et al., 2005), high-frequency stimulation (Toni et al., 2001), glutamate application (Richards et al., 2005), and glutamate uncaging (Ueda and Hayashi, 2013). EM studies suggest that spinules in the teleost retina form in response to Ca^{2+}-dependent synaptic plasticity (Country and Jonz, 2017). We found that Ca^{2+} is crucial for mammalian spinule formation and observed Ca^{2+} nanodomains within spinules isolated from but often in synchrony with spine heads. Short- and long-lived spinules were differentially regulated by Ca^{2+}, and Ca^{2+} signaling was comparatively heightened in long-lived spinules. Future work will determine whether Ca^{2+} enters spinules from the spine head or via channels on the spinule surface.

Our study demonstrates spinule regulation by the key actin cytoskeleton regulatory GEF protein kalirin-7, which promotes spinule formation, elongation, and recurrence. Activation of NMDARs results in CaMKII-dependent phosphorylation of kalirin-7, activation of Rac-1, and spine enlargement (Xie et al., 2007). CaMKII could therefore provide a mechanistic link between Ca^{2+} signaling, kalirin-7 activation, and actin cytoskeletal remodeling in spinule formation. Because the kalirin-7 Sec14p-like domain can interact directly with PIP_3 (Miller et al., 2015), kalirin-7 could also mediate the previously reported PIP_3 regulation of spinule formation (Ueda and Hayashi, 2013). We propose that spinule-driven interactions participate in kalirin-dependent biological processes at synapses; e.g., structural plasticity and synaptogenesis. Our findings are consistent with reports of F-actin- and Rac1-driven spinule formation (Colicos et al., 2001; Chazeau et al., 2014). Alternate regulatory pathways may exist in kalirin isoforms 12 and 9, which contain a second RhoA-specific GTPase binding domain (Penzes et al., 2001). Abnormal kalirin signaling has been associated with schizophrenia (Cahill et al., 2009; Russell et al., 2014) as well as Alzheimer’s disease (Cissé et al., 2017; Xie et al., 2019), and spinule alterations may contribute to these disorders. Suggesting kalirin-independent pathways, pyramidal neurons from mice deficient in KIBRA, a membrane trafficking protein with a role in cognition, exhibit fewer spinules (Blanque et al., 2015). Alterations in spinule length or number have been reported in Parkinson’s disease, amyotrophic lateral sclerosis, and Down syndrome (Anglade et al., 1996; Sasaki and Iwata, 1999; Popov et al., 2011). Future studies should focus on the role of spinules in neuropsychiatric disorders.

Insight into Spinule Functions

Our data suggest that spinules play roles in several aspects of neuronal connectivity. Short-lived, highly dynamic spinules extend and retract repeatedly under basal and activated conditions to function in surveying the local environment for new potential contacts. Spinules can be stabilized in response to signals from active presynaptic terminals, and the resulting long-lived structures may be directly involved in multiple aspects of synapse formation. Elongated filopodia and thin-shaped spinules trafficked PSD fragments or contacted distal presynaptic terminals, but not both, suggesting that they exist as an intermediate state. Mushroom spinules maintained dynamic contact with large distal

terminals in live neurons, and PSD95 puncta colocalized with presynaptic markers at bulbous mushroom spinule tips in fixed neurons, suggesting “mini-synapse” formation.

Although the synapse is conceptualized as a one-to-one connection, “multi-synaptic boutons,” where multiple spines contact one presynaptic terminal, have been reported in the hippocampus, cortex, and cerebellum and have been linked to sensory experience, brain lesions, and learning (Yang et al., 2018). The lesser-known “multi-synaptic spines” receive inputs from multiple presynaptic boutons to form many-to-one connections and have been reported in complex motor learning in rats (Jones et al., 1999), fear conditioning in mice (Yang et al., 2016), and epilepsy (Kuwajima et al., 2013). Intriguingly, a recent study showed that adding synaptic “nanomodule” units modulates experience-dependent structural spine plasticity (Hruska et al., 2018). We propose that contact between spinules and distal presynaptic terminals can lead to stable, secondary synapse and multi-synaptic spine formation, providing additional modality for increasing spine connectivity. Neuronal activation promotes spinule formation, elongation, and contact with distal terminals. These findings are consistent an EM study showing that most spinules project into distal boutons (Sorra et al., 1998), another revealing that spine head protrusions extend toward active presynaptic terminals guided by glutamate release (Richards et al., 2005), and a study showing spinule growth toward new presynaptic actin puncta (Colicos et al., 2001). Alternate or concurrent spinule functions may include presynaptic membrane retrieval via *trans*-endocytosis and/or retrograde signaling (Spacek and Harris, 2004). Our investigation has revealed unexpected diversity in spinule dynamics, lifespan, regulatory mechanisms, and their ability to form connectivity-altering secondary synapses, providing the impetus for studies of spinule function in health and disease.

STAR★METHODS

RESOURCE AVAILABILITY

Lead Contact—Further information and requests should be directed to the Lead Contact, Peter Penzes (p-penzes@northwestern.edu).

Materials Availability—Further information and requests for materials should be directed to and will be fulfilled by the Lead Contact, Peter Penzes, upon request.

Data and Code Availability—This study did not generate code, but datasets related to the current study are available from the Lead Contact, Peter Penzes, upon request.

EXPERIMENTAL MODEL AND SUBJECT DETAILS

Murine dissociated cortical neuron cultures—C57BL6 mice were bred at the Janelia Research campus in accordance with their “Use of Animals in the Advanced Imaging Center Protocol” #15–120 or at Northwestern University in accordance with animal use protocol #IS00001722. Dissociated cortical neurons were prepared from P0 mouse pups. Briefly, pups were sacrificed, and their brains were extracted and placed in cold L-15 medium (Millipore Sigma) plus Penicillin/streptomycin (P/S) solution (GIBCO). Meninges were removed with fine forceps and the cortices dissected with the aid of a dissection microscope

and transferred to cold L-15 media. Media was replaced with pre-warmed 0.25% trypsin (HyClone) and the tubes were placed in 37°C H_20 bath for 10 min. Trypsin was replaced with 1 mL of RF medium, consisting of 426 mL high glucose DMEM (Thermo Fisher Scientific) + 50 mL fetal bovine serum (FBS) (Life Technologies) + 3.5 mL P/S solution + 3.5 mL 100X L-Glutamax (Sigma) + 15 mL sterile filtered 20% D-(+)-glucose (Millipore Sigma). Cells were mechanically dissociated by gentle pipetting, and the cell suspension was passed through a 40 μm nylon cell strainer and plated to 35 mm 1.5 coverslip poly-D-lysine (PDL)-coated glass-bottom imaging dishes (Mattek) that were coated a second time with PDL (0.2 mg/ml, Millipore Sigma) at a density of 1.2×10^6 cells per dish. Dishes were placed in 37°C, 5% CO_2 incubator for 1 hour to allow attachment, and RF media was replaced with neurobasal (NB) media without phenol red (GIBCO) + supplements, i.e., 100X Glutamax I (GIBCO), B27 supplement (Life Technologies), and P/S. Neuronal cultures were maintained in a humidified chamber at 37°C, with 5% CO_2 with NB containing 200 μM D, L-amino-phosphonovalerate (APV) (Abcam), by replacing one half of the media with fresh maintenance media every 3–4 days.

HEK293 culture—HEK293 cells were grown in RPMI-1640 containing 5% fetal bovine serum (Cellgro) with P/S at 37°C with 5% CO_2. They were passaged appropriately during linear growth phase to maintain sub-confluent culture and seeded at 1.5×10^5 cells/well into 12-well plates prior to transfection the next day.

Murine acute brain slice preparation—P31 Thy1-YFP-H mice (Jackson Laboratories) (n = 2; 1 male and 1 female) were sacrificed by cervical dislocation, and their brains were rapidly removed from the skull and placed into ice-cold slicing solution containing (in mM): NaCl 92, KCl 2.5, $CaCl_2$ 0.5, $NaHCO_3$ 30, $MgSO_4$ 10, NaH_2PO_4 1.2, glucose 25, HEPES 20, sodium ascorbate 5, and sodium pyruvate 3, at pH 7.4. The forebrains were quickly dissected, glued down leaning vertically against agar blocks and submerged in cold, oxygenated slicing solution where they were sectioned in 300 μm thick coronal slices using a vibratome (Leica). The slices were preincubated for a minimum of 45 min or until imaging was performed at 37°C in recovery solution containing (in mM), NaCl 92, KCl 2.5, $CaCl_2$ 2, $NaHCO_3$ 30, $MgSO_4$ 2, NaH_2PO_4 1.2, glucose 25, HEPES 20, sodium ascorbate 5, and sodium pyruvate 3, at pH 7.4. Imaging was performed in 37°C in recording artificial cerebrospinal fluid (aCSF) composed of NaCl (in mM) 124, KCl 2.5, $CaCl_2$ 2, $NaHCO_3$ 24, $MgSO_4$ 1, NaH_2PO_4 1.2, glucose 12.5, HEPES 5, pH 7.4. All the solutions were pre-bubbled with 95% O_2/5% CO_2 gas mixture for at least 30 min to ensure O_2 saturation before slice immersion. For confocal imaging, a coverslip was assembled into an imaging chamber where the slices were immobilized with *a harp* placed against the coverslip glass and perfused with recording aCSF. Somatosensory M2 layer V pyramidal neurons were located using a 2X objective prior to confocal imaging.

METHOD DETAILS

Plasmids and transfections of cultured neurons—Chemical transfections of cultured neurons were performed at 37°C with 5% CO_2 in NB plus supplements media without P/S. First, 7 μl of Lipofectamine 2000 (LFA2K) (Thermo Fisher Scientific) was added to 100 μl Opti-MEM 1X (GIBCO), and plasmid DNA was added to 50 μl of Opti-

MEM (per dish). LFA2K and plasmid DNA were mixed into 1 tube and incubated for 20–30 min at 37°C. For each dish, conditioned media was replaced with antibiotic-free NB and the DNA complexes were added and incubated for 4 hours, when the media was replaced with half conditioned media and half fresh NB plus supplements. Dishes were incubated for 2–3 days, depending on the experiment, to allow for adequate expression of plasmid-encoded fluorescent proteins or shRNAs. For rapid SIM studies, we used 3.5 μg of DNA pDsRedExpress2-N1 (Clontech). For confocal studies of the PSD and spinule dynamics, we used 3.5 μg of p-mRuby-N1 plasmid, a gift from Michael Davidson (Addgene #54581) + 3.5 μg of pCAG_PSD95.FingR-eGFP-CCR5TC, a gift from Don Arnold (Addgene #46295). For Ca^{2+} transients experiments, we used 3.5 μg p-mRuby-N1 + 3.5 μg pGP-CMV-GCaMP6s, a gift from Douglas Kim, GENIE Project (Addgene #40753). Four μg of p-mRuby-N1 alone was used in the FM dye labeling experiments, and pGFP, a gift from Stephen Mayfield (Addgene #64904), was added at 2 μg per neuronal coverslip for fixed imaging experiments.

Lentiviral and AAV plasmids—The kalirin-7 exogenous expression plasmid (pLV-Kal-7 mCherry) was generated by VectorBuilder. The kalirin-7 sequence (NM_001164268.1) was inserted into a lentivirus plasmid containing an mCherry tag driven by a synapsin promoter. The kalirin-7 sequence was separated from the mCherry tag by a P2A cleavage site to ensure the tag did not alter the function of kalirin-7. A plasmid containing all but the kalirin-7 and P2A site served as a control (pLV-mCherry). To generate the pAAV-shKal-7 GFP plasmid, the Kal-7 shRNA sequence GCAGTACAATCCTGGCCATGT (Xie et al., 2010) was ordered from OriGene, along with a standard scramble sequence to serve as a control. The shRNA and scramble sequences were then packaged into an AAV plasmid containing a GFP tag driven by a CMV promoter (pGFP-A-shAAV).

HEK293 transfection and immunoblot—The efficiencies of the pAAV-shKal-7 GFP and the pLV-Kal-7 mCherry plasmids were tested in HEK cells. Cultures were transfected for 3 days in antibiotic-free RPMI media at approximately 30% confluence using 4 μl of Lipofectamine 2000 (Thermo Fisher Scientific) and a total of 4 μg of DNA (1 μg pLV-Kal-7 mCherry or pLV-mCherry as a control) and 3 ug pAAV-shKal-7 GFP (or pAAV-scramble-GFP as a control). Cells were then harvested in RIPA buffer (10 mM TRIS pH 7.2, 15 mM NaCl, 1% DOC, 1% Triton, 0.1% SDS, 1 Roche complete protease cocktail inhibitor tablet) and analyzed by SDS-PAGE and western blotting using standard methods. Briefly, equal amounts of protein were separated by SDS-PAGE 7.5% gradient tris-glycine gels (Bio-Rad). Following transfer to PVDF membrane, blots were blocked with 5% BSA for 1 hour, incubated first with primary antibodies (kalrn (goat) 1:500 (Abcam), actin (rabbit) 1:5000 (US Biological Life Sciences)) and then with horseradish peroxidase secondary antibodies (anti-goat 1:10,000, anti-rabbit 1:10,000 (Jackson ImmunoResearch Laboratories). Immunoreactivity was evaluated using a chemiluminescent reagent (Pierce) and measured using a ChemiDoc imaging system (Bio-Rad).

Neuronal culture treatments and reagents—For Ca^{2+} transients experiments, DIV 19 mouse cortical neurons were transfected with mRuby and GCaMP6s plasmids. After 2 days to allow for sufficient plasmid expression, NB media was replaced with pre-warmed 1X ACSF (Smith et al., 2014) and incubated at 37°C for 30 min. In each dish, media was

replaced with pre-warmed 1X ACSF + 20 μm BAPTA-AM diluted in DMSO (Sigma-Aldrich), or the equivalent volume of DMSO alone (0.5 μl/ml) for the treatment and negative control group, respectively. After a 30 min treatment at 37°C in 5% CO_2, live imaging was conducted on 1 stage position per dish.

To validate FM dyes for labeling active presynaptic terminals in neuronal cultures, FM 1–43 Dye (N-(3-Triethylammoniumpropyl)-4-(4-(Dibutylamino) Styryl) Pyridinium Dibromide) (Thermo Fisher Scientific) was reconstituted in sterile H_2O prior to use. Coverslips of DIV 21 mRuby-expressing neurons were transferred from conditioned NB media into HBSS with Ca^{2+} and Mg^{2+} (Thermo Fisher Scientific) with or without 50 μM of the dynamin inhibitor, Dynasore (Tocris), for 10 min as a pre-treatment. Coverslips were then labeled for 90 s with HBSS only (control), 60 mM KCl (Sigma) in HBSS, or 60 mM KCl + 50 μM Dynasore in HBSS, and washed 3 times with HBSS before returning to conditioned NB for imaging (data not shown). For experimental conditions, the media was replaced with warm HBSS with Ca^{2+} and Mg^{2+} + 200 μM APV and incubated for 10 min, then replaced with warm HBSS + 60 mM KCl + 5 μg/ml FM1–43 for 90 s, washed 3 times in HBSS, returned to conditioned NB, and then imaged.

Acute NMDAR activation by APV withdrawal has been described previously (Xie et al., 2007). Briefly, pGFP-transfected neurons were maintained in NB media with 200 μM APV until DIV 21. Culture media was replaced with fresh NB media with or without 200 μM APV for 30 min prior to chemical fixation.

Immunocytochemistry—Basal state GPF-transfected neurons to be stained for PSD95 and a presynaptic marker were washed with 0.1 M phosphate buffered saline (1X PBS) and fixed with 4% formaldehyde (Sigma) in 4% sucrose/PBS for 15 min at room temperature (RT). Primary and secondary antibodies were diluted in PBS containing 4% bovine serum albumin (BSA) (Fisher Scientific) and 5% normal goat serum (NGS) (Jackson Immunoresearch). As described previously (Gao et al., 2019), cells were permeabilized and blocked simultaneously in PBS containing 0.1% Triton, 5% NGS, and 4% BSA for 2 hours at 4°C, followed by incubation at 4°C overnight with primary antibodies at 1:1000, i.e., monoclonal mouse PSD95 (NeuroMab) and polyclonal Guinea pig VGLUT1 (Synaptic Systems). Cells were then washed 3 times with PBS and incubated for 1 hour at RT with secondary antibodies at 1:1000, i.e., goat anti-mouse Alexa Fluor 568 and goat anti-Guinea pig Alexa Fluor 647 (Thermo Fisher Scientific), and washed 3 times with PBS. Coverslips were briefly rinsed in distilled water and mounted onto microscopy slides using Prolong Gold Antifade Mountant (Thermo Fisher Scientific).

Basal and activated state GFP-transfected neurons to be stained for a presynaptic marker and F-actin were washed with 1X PBS and fixed using Image-iT Fixative Solution (Thermo Fisher Scientific), a methanol-free PBS solution with 4% formaldehyde for 15 min at RT. This modified protocol was used to better preserve F-actin. Neurons were permeabilized and blocked simultaneously with 0.1% Triton, 5% NGS, and 4% BSA, followed by incubation with polyclonal Guinea pig anti-bassoon primary antibodies (Synaptic Systems) at 1:1000, as described previously. Coverslips were washed and treated for 1 hour at RT with goat anti-Guinea pig Alexa Fluor 568 secondary antibodies (Thermo Fisher Scientific) at 1:1000.

Coverslips were additionally stained with Alexa Fluor 647 Phalloidin (Thermo Fisher Scientific) at a final concentration of 6.5 μM for 30 min prior to washing and mounting onto slides as described previously.

Microscopy and image processing—Imaging of dissociated neurons was conducted at 21 DIV in an environmental imaging chamber at 37°C with 5% CO_2. Image fields were selected on secondary branches of apical dendrites on excitatory pyramidal neurons that showed no signs of poor health, e.g., membrane blebbing. In Ca^{2+} experiments, control neurons were first selected at 20X magnification if they displayed observable spontaneous Ca^{2+} transients and showed no signs of membrane blebbing. Researchers were blinded prior to image acquisition in experiments comparing two or more treatment groups.

High-speed 3D SIM: Experiments were performed at the Advanced Imaging Center (AIC) of the Janelia Research Campus on a custom-built SIM system that enabled rapid acquisition of optical sections by employing a liquid crystal spatial light modulator with a rapid-switching variable retarder to efficiently alter the grating pattern, as described previously (Kner et al., 2009; Li et al., 2015). Images were collected using a 100X 1.46 NA Zeiss oil objective and a 560 nm excitation laser at the following 3D pixel dimensions: x = 0.04 μm, y = 0.04 μm, z = 0.15 μm. Z stack intervals were collected at 15–20 s per frame depending on the number of slices, ranging from 19 to 21, at a 0.1 μm step size. This interval included a 7–10 s imaging period and an equal recovery period to minimize the rate of photo-bleaching and extend the imaging duration for quantitation of long-lived spinules. For this system, the AIC reported a lateral resolution of 110 nm and an axial resolution of 360 nm (at 488 nm excitation). Notably, the enhanced acquisition speed compared to standard SIM results in fewer motion artifacts. Raw, rapid SIM datasets were reconstructed using a custom algorithm provided by Janelia researchers, and reconstructions were then imported into ImageJ-Fiji to convert from 32- to 16-bit images for further analysis.

Enhanced resolution confocal microscopy: In instances that required endogenous protein labeling, less photo-bleaching, and/or increased speed than could be achieve by SIM, we utilized enhanced resolution confocal microscopy. Images were acquired using a Nikon A1R with resonant scanning and a GaAsP multi-detector unit using a 100X 1.45 NA Plan Apo Lambda oil objective and 488 and 561 nm excitation lasers. To approach the system's optical limit, we adjusted the pinhole to 0.6 airy units, and selected a pixel size of 1/2 nyquist using the following 3D pixel dimensions: x = 0.06 μm, y = 0.06 μm, z = 0.12 μm. Z-intervals ranged from 0.1 to 0.12 μm. For the Nikon A1R system, the calculated lateral resolution limit was 139 nm and the axial resolution was 349 nm. To achieve enhanced resolution, we also utilized iterative image restoration-based 3D deconvolution software, which can afford up to a ~1.5 times improvement in xy and a ~1.7 times improvement in z (Holmes and Liu, 1989; Biggs, 2010). For the experiments performed on neurons expressing mRuby and PSD95-specific intrabodies, a total of 41 to 43 slices were acquired with averaging at z stack intervals between 8.2 and 8.47 s. Bleach correction was applied to both channels using ImageJ-Fiji. For experiments performed on neurons expressing mRuby and GCaMP6s, 25 slices were acquired at a z stack interval of 2.2 s. In these datasets, only the red channel was deconvolved and bleach corrected, so as not to alter GCaMP6 MFI utilized in the Ca^{2+} $\Delta F/F_0$ quantitation. For kalirin-7 exogenous expression and knock-down

experiments, z-intervals ranged from 19.3 to 27 s, and from 19.5 to 28.1 s, respectively. The imaging duration was 10 minutes, from which the first 5 minutes was analyzed.

Images of PSD95 and VGLUT1 immunostained neurons were acquired using a 63X oil immersion objective lens on a Nikon C2+ confocal microscope with NIS-Elements software. Each channel was acquired sequentially to prevent fluorescence bleed-through with 2x line averaging for each channel. Neurons were imaged on multiple z-planes to capture full dendritic branches. Post imaging acquisition 3D deconvolution was performed to enhance spinule detection prior to analysis, as described previously.

QUANTIFICATION AND STATISTICAL ANALYSIS

Sample selection—For each experiment, neurons were derived from 2 or more independent culture preparations. Large volumetric SIM datasets were obtained from 2 neurons, and smaller volumetric datasets obtained by enhanced resolution microscopy were from 8 neurons for PSD imaging, as well as 11 vehicle-treated neurons and 10 BAPTA-AM-treated neurons for Ca^{2+} imaging. In the Kalirin-7 overexpression and knock-down experiments, neurons were derived from 3 independent culture preparations, analyzing 18 kalirin-7-expressing neurons and 15 (−)control neurons, as well as 10 kalirin-7 knock-down and 8 scramble neurons. Neurons used in the immunocyto-chemistry (ICC) experiment to label pre- and postsynaptic markers in basal state neurons was from 2 independent preparations and 10 neurons were analyzed. The ICC experiment comparing presynaptic terminal and F-actin-labeled basal versus activated neurons was from 3 independent preparations, with 20 control neurons and 24 NMDAR-activated neurons analyzed. Acute brain slices were prepared from 2 mice, and 2 healthy YFP-transfected layer V somatosensory cortical neurons were imaged per brain. For all experiments, dendritic spine and spinule numbers analyzed in each condition are indicated in the figure captions. Spines were excluded from further analysis if their entirety was not captured within the field of view in all z stacks analyzed.

Quantification of spines and spinules—Quantification of spine class, spine and spinule volumes, spinule number, and spinule lifespan over time was performed in 3D using Imaris imaging analysis software versions 8.4.1–9.5.0 (Bitplane), unless otherwise specified. When assessing two or more treatment groups, data analysts were blinded. Three-dimensional volume view videos were also constructed using Imaris. A mushroom spine was defined as one with a large head much greater in diameter than the neck, while filopodia were defined as a long, thin dendritic projection with no head, and thin spines were those with a long thin neck and small head (Harris et al., 1992). A transitioning spine was defined as one that changed class, e.g., from filopodia to thin, during the imaging duration. Spines closely associated with adjacent labeled neuronal elements were excluded from volume analysis by necessity. Since mushroom spines predominantly formed spinules, we excluded other spine subtypes, e.g., thin spines, from our subsequent in-depth analyses.

A spinule was generally defined as a thin membranous projection of the mushroom spine that was at least 0.2 μm in length. An individual spinule was defined as one that existed in a single z stack or in consecutive stacks (time points), and lifespan was calculated as the

number of stacks in which a spinule was consecutively detected at a specific spine head location multiplied by the number of s per stack. Spinule lengths were measured from base to tip and widths measured at the narrowest point of the spinule from stack to stack. We observed that the widths of spinule-like projections were often not uniform along their length and undulated over time, so we chose to include thicker structures (< 0.3 μm), provided that the length was greater than the width. Mean length, width, and volume measurements represent the average across all frames in which a spinule appeared consecutively. Individual tracking of spinule lifespans over time in live confocal imaging data was achieved in 3D using Imaris and spinule length measurements obtained using Imaris Measurement Pro Module. ImageJ-Fiji was used to obtain spinule length and width measurements from maximum projections in rapid SIM datasets, and spinule lengths in ICC datasets.

Spinule recurrence—We first normalized the spinule origination point across the mushroom spine head to objectively quantitate recurrence in SIM datasets, considering that spines can rapidly change their shape and size and exhibit dynamic motility, including changes in spine head location relative to the dendritic shaft. In projection images, we traced the outline of the spine head ~0.1 μm from the edge at each time point and generated single frame kymographs (plot profiles) of fluorescence intensity, with each peak in intensity signifying a spinule intersection and origination point. The length of each plot profile was then normalized on a generic unit scale of 0–100 to normalize the location, which was used to generate spatio-temporal plots to track spinule recurrence (within 10 units) in non-continuous frames in each spine. One outlier spinule had a lifespan that equaled or exceeded the duration of imaging, so recurrence could not be assessed, and this spinule was excluded from the analysis. In enhanced resolution confocal datasets, recurrence was tracked stack by stack in 3D using the Imaris Measurement Pro Module.

Spinule origin relative to the PSD—In addition to spinule lengths, the distance from the spinule origination, i.e., base of the spinule, to the nearest edge of the PSD, was measured over time in 3D using the Imaris Measurement Pro Module. The PSD edge was defined by GFP fluorescence detected in neurons expressing PSD95-specific GFP-tagged intrabodies, and the mRuby cell-fill labeled neuronal elements. To follow PSD volume and mean number of PSD fragments in individual dendritic spines stack by stack, we utilized Imaris Surfaces with tracking, based on absolute GFP intensity of bleach-corrected images. PSDs were classified as partitioned if they displayed a moderate to high degree of segmentation and/or fragments over time, ie. in ≥ 50% of z stacks. PSDs were classified as fragmented if > 1 separate PSD volumes were detected in ≥ 10% of stacks using Imaris object tracking. The mean and maximum fragment number per stack was calculated objectively using Imaris surfaces with tracking using a consistent threshold based on absolute GFP intensity.

Calcium transients—For experiments performed on neurons expressing an mRuby cell-fill and GCaMP6s, only the red channel was deconvolved, a maximum intensity projection generated for each stack, and alignment of the red channel was achieved using NIS Elements. Regions of interest (ROIs) were drawn using the ROI editor within the dendritic

shaft adjacent to the spine, spine head, and spinules, where possible. Those neuronal elements in close contact with other neuronal structures, which could not be adequately differentiated, were excluded from further analysis. ROIs were adjusted stack by stack and mean GCaMP6 MFI (raw AU) was calculated in NIS Elements for each of the 137 z stacks. From the MFI values, the $\Delta F/F_0$ ratio was calculated by first averaging the values from 4–5 frames collected during an early period of inactivity to calculate F_0, and then deriving ΔF from the following equation: $\Delta F = F(t) - F_0$. Ca^{2+} peaks were defined as $\Delta F/F_0 > 0.5$ or a 50% fluorescence increase over baseline. An individual peak $\Delta F/F_0$ maximum was defined as the highest value in a string of values above 0.5, and the peak duration defined as the number of s spanned by a string of ascending and then descending values (over 0.5) around the maximum. Mean and maximum Ca^{2+} peak $\Delta F/F_0$ per spine refers to the average or maxima of all peaks detected in that spine over 300 s of imaging. To directly assess Ca^{2+} transients in co-occurrent short-versus long-lived spinules, we compared GCaMP6 MFI in instances where a short- and long-lived spinule existed in the same spine in the same stack (time point) during periods of spine head Ca^{2+} inactivity and activity.

Analysis of immunocytochemical stains—Deconvolved confocal images were first assessed in 3D using Imaris for their inclusion in a more detailed analysis. Using ImageJ-Fiji, two-dimensional maximum projections were used to quantify thresholded spine areas and detect the presence of pre- and/or postsynaptic markers closely opposing or colocalizing with the spine head. Spinules were assessed as positive for PSD95 fragments if the spinule and fragment colocalized. Spinules were designated to be contacting presynaptic markers (VGLUT1 or Bassoon) if the thresholded presynaptic puncta directly opposed or colocalized with the spinule. For the theoretical calculation of bassoon contact number within the spine versus the spine + spinule reach, the number of bassoon puncta within the spine perimeter circumference was compared to that of the spine + spinule perimeter circumference. Axons, marked by phalloidin staining, were traced and the number of crossing axons in the inner and outer perimeter circumferences for each spinule(+) spine was quantified similarly. Images with diffuse phalloidin staining were excluded from this analysis by necessity.

Statistics—Statistical analysis was performed using GraphPad Prism Version 8.3. To determine the appropriate statistical test, normality of each distribution was first tested using the D'Agostino-Pearson test. Parameters between 2 independent groups were compared using two-tailed unpaired Student's t tests for normal distributions, or the Mann-Whitney test for non-normal distributions. When the two groups for comparison were related, e.g., the number of short-versus long-lived spinules per spine, a two-tailed paired Student's t test was applied to normally distributed data, and the Wilcoxon matched pairs rank test was used for non-normally distributed data. For comparisons involving more than two independent groups, one-way ANOVA was applied to normally distributed data, or Kruskal Wallis and Dunn's Multiple Comparison test for non-normal distributions. To determine correlation between 2 variables, normally distributed data was assessed using Pearson's correlation, while Spearman's rank correlation was used for non-normally distributed data (with two-tailed permutation tests for significance). The Chi-square test or Fisher's exact test, when the sample size was small, was used to analyze contingency tables of ≥ 2 subgroups and ≥ 2 outcomes. The number of cells and spines and/or spinules (n) is reported in the figure

legends. Data are represented as mean ± SEM. *p < 0.05, **p < 0.01, ***p < 0.001, ****p < 0.0001.

Supplementary Material

Refer to Web version on PubMed Central for supplementary material.

ACKNOWLEDGMENTS

SIM was performed at the Advanced Imaging Center on Janelia's Research Campus. Confocal microscopy was performed at Northwestern's Center for Advanced Microscopy, supported by NCI CCSG P30 CA060553 (to the Robert H. Lurie Comprehensive Cancer Center) and with support from Drs. Arvanitis and Kirchenbuechler. This work was supported by NIH grants R01MH071316 and R01MH107182.

REFERENCES

Anglade P, Mouatt-Prigent A, Agid Y, and Hirsch E (1996). Synaptic plasticity in the caudate nucleus of patients with Parkinson's disease. Neurodegeneration 5, 121–128. [PubMed: 8819132]

Biggs DS (2010). 3D deconvolution microscopy. Curr. Protoc. Cytom. Chapter 12, Unit 1219, 1–20.

Blanque A, Repetto D, Rohlmann A, Brockhaus J, Duning K, Pavenstädt H, Wolff I, and Missler M (2015). Deletion of KIBRA, protein expressed in kidney and brain, increases filopodial-like long dendritic spines in neocortical and hippocampal neurons in vivo and in vitro. Front. Neuroanat 9, 13. [PubMed: 25750616]

Bourne JN, and Harris KM (2008). Balancing structure and function at hippocampal dendritic spines. Annu. Rev. Neurosci 31, 47–67. [PubMed: 18284372]

Cahill ME, Xie Z, Day M, Photowala H, Barbolina MV, Miller CA, Weiss C, Radulovic J, Sweatt JD, Disterhoft JF, et al. (2009). Kalirin regulates cortical spine morphogenesis and disease-related behavioral phenotypes. Proc. Natl. Acad. Sci. USA 106, 13058–13063. [PubMed: 19625617]

Chazeau A, Mehidi A, Nair D, Gautier JJ, Leduc C, Chamma I, Kage F, Kechkar A, Thoumine O, Rottner K, et al. (2014). Nanoscale segregation of actin nucleation and elongation factors determines dendritic spine protrusion. EMBO J. 33, 2745–2764. [PubMed: 25293574]

Chen TW, Wardill TJ, Sun Y, Pulver SR, Renninger SL, Baohan A, Schreiter ER, Kerr RA, Orger MB, Jayaraman V, et al. (2013). Ultrasensitive fluorescent proteins for imaging neuronal activity. Nature 499, 295–300. [PubMed: 23868258]

Cissé M, Duplan E, and Checler F (2017). The transcription factor XBP1 in memory and cognition: Implications in Alzheimer disease. Mol. Med 22, 905–917. [PubMed: 28079229]

Colicos MA, Collins BE, Sailor MJ, and Goda Y (2001). Remodeling of synaptic actin induced by photoconductive stimulation. Cell 107, 605–616. [PubMed: 11733060]

Country MW, and Jonz MG (2017). Calcium dynamics and regulation in horizontal cells of the vertebrate retina: lessons from teleosts. J. Neurophysiol 117, 523–536. [PubMed: 27832601]

Cox S (2015). Super-resolution imaging in live cells. Dev. Biol 401, 175–181. [PubMed: 25498481]

Dhanrajan TM, Lynch MA, Kelly A, Popov VI, Rusakov DA, and Stewart MG (2004). Expression of long-term potentiation in aged rats involves perforated synapses but dendritic spine branching results from high-frequency stimulation alone. Hippocampus 14, 255–264. [PubMed: 15098730]

Erisir A, and Dreusicke M (2005). Quantitative morphology and postsynaptic targets of thalamocortical axons in critical period and adult ferret visual cortex. J. Comp. Neurol 485, 11–31. [PubMed: 15776444]

Fiolka R, Shao L, Rego EH, Davidson MW, and Gustafsson MG (2012). Time-lapse two-color 3D imaging of live cells with doubled resolution using structured illumination. Proc. Natl. Acad. Sci. USA 109, 5311–5315. [PubMed: 22431626]

Gao R, Zaccard CR, Shapiro LP, Dionisio LE, Martin-de-Saavedra MD, Piguel NH, Pratt CP, Horan KE, and Penzes P (2019). The CNTNAP2-CASK complex modulates GluA1 subcellular distribution in interneurons. Neurosci. Lett 701, 92–99. [PubMed: 30779956]

Godin AG, Lounis B, and Cognet L (2014). Super-resolution microscopy approaches for live cell imaging. Biophys. J 107, 1777–1784. [PubMed: 25418158]

Gross GG, Junge JA, Mora RJ, Kwon HB, Olson CA, Takahashi TT, Liman ER, Ellis-Davies GC, McGee AW, Sabatini BL, et al. (2013). Recombinant probes for visualizing endogenous synaptic proteins in living neurons. Neuron 78, 971–985. [PubMed: 23791193]

Harris KM, Jensen FE, and Tsao B (1992). Three-dimensional structure of dendritic spines and synapses in rat hippocampus (CA1) at postnatal day 15 and adult ages: implications for the maturation of synaptic physiology and long-term potentiation. J. Neurosci 12, 2685–2705. [PubMed: 1613552]

Holmes TJ, and Liu YH (1989). Richardson-Lucy/maximum likelihood image restoration algorithm for fluorescence microscopy: further testing. Appl. Opt 28, 4930–4938. [PubMed: 20555971]

Hotulainen P, and Hoogenraad CC (2010). Actin in dendritic spines: connecting dynamics to function. J. Cell Biol 189, 619–629. [PubMed: 20457765]

Hruska M, Henderson N, Le Marchand SJ, Jafri H, and Dalva MB (2018). Synaptic nanomodules underlie the organization and plasticity of spine synapses. Nat. Neurosci 21, 671–682. [PubMed: 29686261]

Jones TA, Chu CJ, Grande LA, and Gregory AD (1999). Motor skills training enhances lesion-induced structural plasticity in the motor cortex of adult rats. J. Neurosci 19, 10153–10163. [PubMed: 10559423]

Kner P, Chhun BB, Griffis ER, Winoto L, and Gustafsson MG (2009). Super-resolution video microscopy of live cells by structured illumination. Nat. Methods 6, 339–342. [PubMed: 19404253]

Kuwajima M, Spacek J, and Harris KM (2013). Beyond counts and shapes: studying pathology of dendritic spines in the context of the surrounding neuropil through serial section electron microscopy. Neuroscience 251, 75–89. [PubMed: 22561733]

Lauterbach MA, Guillon M, Desnos C, Khamsing D, Jaffal Z, Darchen F, and Emiliani V (2016). Superresolving dendritic spine morphology with STED microscopy under holographic photostimulation. Neurophotonics 3, 041806. [PubMed: 27413766]

Li D, Shao L, Chen BC, Zhang X, Zhang M, Moses B, Milkie DE, Beach JR, Hammer JA 3rd, Pasham M, et al. (2015). ADVANCED IMAGING. Extended-resolution structured illumination imaging of endocytic and cytoskeletal dynamics. Science 349, aab3500. [PubMed: 26315442]

Ma XM, Johnson RC, Mains RE, and Eipper BA (2001). Expression of kalirin, a neuronal GDP/GTP exchange factor of the trio family, in the central nervous system of the adult rat. J. Comp. Neurol 429, 388–402. [PubMed: 11116227]

Medvedev NI, Popov VI, Rodriguez Arellano JJ, Dallérac G, Davies HA, Gabbott PL, Laroche S, Kraev IV, Doyère V, and Stewart MG (2010). The N-methyl-D-aspartate receptor antagonist CPP alters synapse and spine structure and impairs long-term potentiation and long-term depression induced morphological plasticity in dentate gyrus of the awake rat. Neuroscience 165, 1170–1181. [PubMed: 19961908]

Miller MB, Vishwanatha KS, Mains RE, and Eipper BA (2015). An N-terminal Amphipathic Helix Binds Phosphoinositides and Enhances Kalirin Sec14 Domain-mediated Membrane Interactions. J. Biol. Chem 290, 13541–13555. [PubMed: 25861993]

Murphy DD, and Andrews SB (2000). Culture models for the study of estradiol-induced synaptic plasticity. J. Neurocytol 29, 411–417. [PubMed: 11424957]

Nägerl UV, Willig KI, Hein B, Hell SW, and Bonhoeffer T (2008). Live-cell imaging of dendritic spines by STED microscopy. Proc. Natl. Acad. Sci. USA 105, 18982–18987. [PubMed: 19028874]

Okabe S, Kim HD, Miwa A, Kuriu T, and Okado H (1999). Continual remodeling of postsynaptic density and its regulation by synaptic activity. Nat. Neurosci 2, 804–811. [PubMed: 10461219]

Pappas GD, and Purpura DP (1961). Fine structure of dendrites in the superficial neocortical neuropil. Exp. Neurol 4, 507–530. [PubMed: 14483755]

Penzes P, Johnson RC, Kambampati V, Mains RE, and Eipper BA (2001). Distinct roles for the two Rho GDP/GTP exchange factor domains of kalirin in regulation of neurite growth and neuronal morphology. J. Neurosci 21, 8426–8434. [PubMed: 11606631]

Petralia RS, Wang YX, Mattson MP, and Yao PJ (2015). Structure, Distribution, and Function of Neuronal/Synaptic Spinules and Related Invaginating Projections. Neuromolecular Med. 17, 211–240. [PubMed: 26007200]

Petralia RS, Wang YX, Mattson MP, and Yao PJ (2018). Invaginating Structures in Mammalian Synapses. Front. Synaptic Neurosci 10, 4. [PubMed: 29674962]

Popov VI, Kleschevnikov AM, Klimenko OA, Stewart MG, and Belichenko PV (2011). Three-dimensional synaptic ultrastructure in the dentate gyrus and hippocampal area CA3 in the Ts65Dn mouse model of Down syndrome. J. Comp. Neurol 519, 1338–1354. [PubMed: 21452200]

Richards DA, Mateos JM, Hugel S, de Paola V, Caroni P, Gähwiler BH, and McKinney RA (2005). Glutamate induces the rapid formation of spine head protrusions in hippocampal slice cultures. Proc. Natl. Acad. Sci. USA 102, 6166–6171. [PubMed: 15831587]

Russell TA, Blizinsky KD, Cobia DJ, Cahill ME, Xie Z, Sweet RA, Duan J, Gejman PV, Wang L, Csernansky JG, and Penzes P (2014). A sequence variant in human KALRN impairs protein function and coincides with reduced cortical thickness. Nat. Commun 5, 4858. [PubMed: 25224588]

Sasaki S, and Iwata M (1999). Ultrastructural change of synapses of Betz cells in patients with amyotrophic lateral sclerosis. Neurosci. Lett 268, 29–32. [PubMed: 10400070]

Smith KR, Kopeikina KJ, Fawcett-Patel JM, Leaderbrand K, Gao R, Schürmann B, Myczek K, Radulovic J, Swanson GT, and Penzes P (2014). Psychiatric risk factor ANK3/ankyrin-G nanodomains regulate the structure and function of glutamatergic synapses. Neuron 84, 399–415. [PubMed: 25374361]

Sorra KE, Fiala JC, and Harris KM (1998). Critical assessment of the involvement of perforations, spinules, and spine branching in hippocampal synapse formation. J. Comp. Neurol 398, 225–240. [PubMed: 9700568]

Spacek J, and Harris KM (2004). Trans-endocytosis via spinules in adult rat hippocampus. J. Neurosci 24, 4233–4241. [PubMed: 15115819]

Stewart MG, Medvedev NI, Popov VI, Schoepfer R, Davies HA, Murphy K, Dallérac GM, Kraev IV, and Rodríguez JJ (2005). Chemically induced long-term potentiation increases the number of perforated and complex postsynaptic densities but does not alter dendritic spine volume in CA1 of adult mouse hippocampal slices. Eur. J. Neurosci 21, 3368–3378. [PubMed: 16026474]

Tao-Cheng JH, Dosemeci A, Gallant PE, Miller S, Galbraith JA, Winters CA, Azzam R, and Reese TS (2009). Rapid turnover of spinules at synaptic terminals. Neuroscience 160, 42–50. [PubMed: 19248820]

Tarrant SB, and Routtenberg A (1977). The synaptic spinule in the dendritic spine: electron microscopic study of the hippocampal dentate gyrus. Tissue Cell 9, 461–473. [PubMed: 337572]

Toni N, Buchs PA, Nikonenko I, Povilaitite P, Parisi L, and Muller D (2001). Remodeling of synaptic membranes after induction of long-term potentiation. J. Neurosci 21, 6245–6251. [PubMed: 11487647]

Ueda Y, and Hayashi Y (2013). PIP_3 regulates spinule formation in dendritic spines during structural long-term potentiation. J. Neurosci 33, 11040–11047. [PubMed: 23825409]

Westrum LE, and Blackstad TW (1962). An electron microscopic study of the stratum radiatum of the rat hippocampus (regio superior, CA 1) with particular emphasis on synaptology. J. Comp. Neurol 119, 281–309. [PubMed: 14000149]

Xie Z, Srivastava DP, Photowala H, Kai L, Cahill ME, Woolfrey KM, Shum CY, Surmeier DJ, and Penzes P (2007). Kalirin-7 controls activity-dependent structural and functional plasticity of dendritic spines. Neuron 56, 640–656. [PubMed: 18031682]

Xie Z, Cahill ME, and Penzes P (2010). Kalirin loss results in cortical morphological alterations. Mol. Cell. Neurosci 43, 81–89. [PubMed: 19800004]

Xie Z, Shapiro LP, Cahill ME, Russell TA, Lacor PN, Klein WL, and Penzes P (2019). Kalirin-7 prevents dendritic spine dysgenesis induced by amyloid beta-derived oligomers. Eur. J. Neurosci 49, 1091–1101. [PubMed: 30565792]

Yang Y, Liu DQ, Huang W, Deng J, Sun Y, Zuo Y, and Poo MM (2016). Selective synaptic remodeling of amygdalocortical connections associated with fear memory. Nat. Neurosci 19, 1348–1355. [PubMed: 27595384]

Yang Y, Lu J, and Zuo Y (2018). Changes of Synaptic Structures Associated with Learning, Memory and Diseases. Brain Science Advances 4, 99–117.

Highlights

- Most spinules are short-lived, dynamic, recurrent, and originate near simple PSDs
- An elongated stable subset traffics PSD fragments and can form secondary synapses
- Spinule subsets are positively regulated by local Ca^{2+} transients and kalirin-7
- Neuronal activity induces spinule elongation and contact with distal synapses

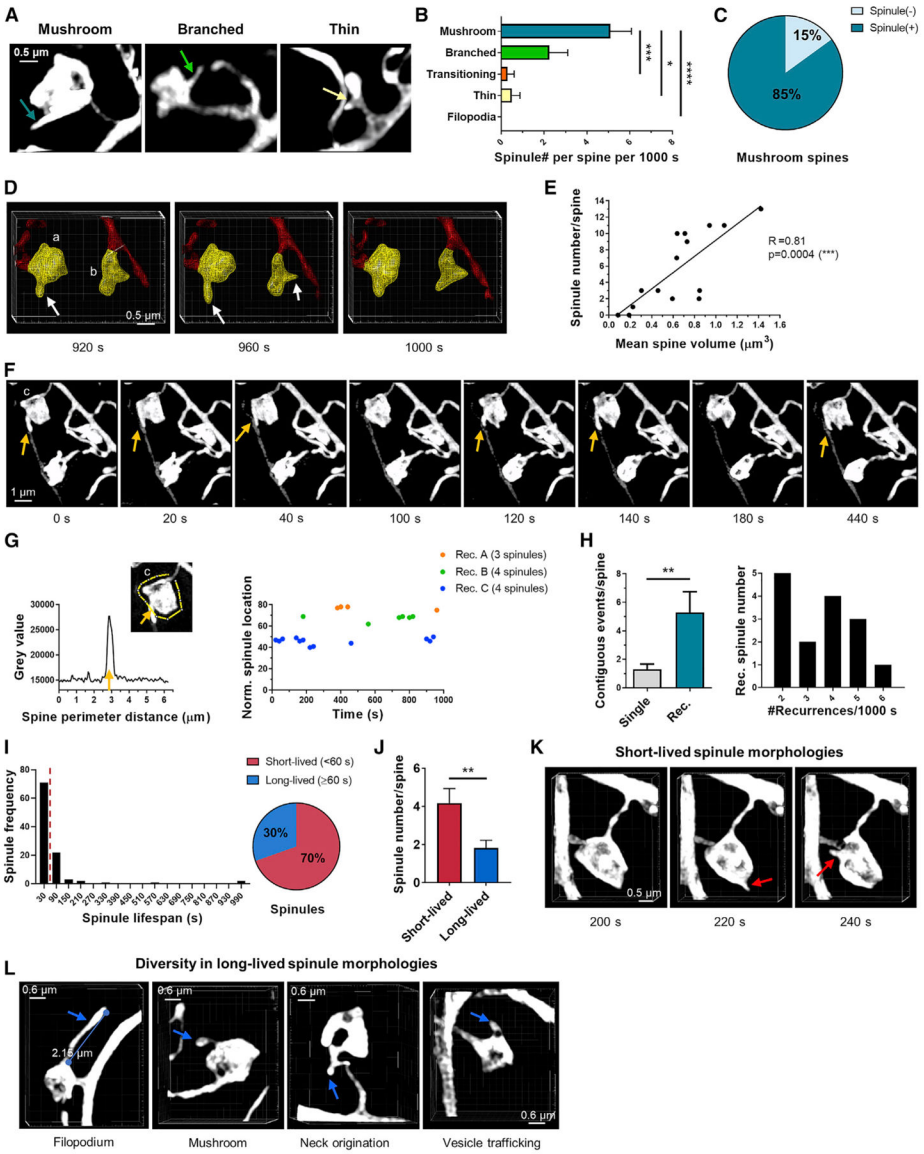

Figure 1. Spinule Recurrence and Divergent Lifespans

(A) Representative 3D SIM constructions of spine classes displaying spinules (arrows).

(B) Spinule number per spine, separated by class (n = 54), over 1000 s. Kruskal-Wallis test; mushroom versus transitioning p = 0.0009, thin p = 0.0153, and filopodia p < 0.0001.

(C) Percentage of spinule(+) and (−) mushroom spines (n = 20) over time.

(D) Wireframe Imaris reconstructions of a representative high-volume spine (a) with spinules (arrows) in multiple z stacks and low-volume spine (b) with a spinule in one stack.

(E) Linear regression and Spearman correlation between spinule number and spine volume (n = 15).

(F) Montage of a spinule (arrows) extending along an axon and recurring at one topographical location. See also Video S1.

(G) Normalized temporal location mapping of three recurrent spinules from spine (c).

(H) Comparison of single versus recurring spinule numbers per spine (n = 66). Unpaired Student's t test, p = 0.0152. The histogram shows the number of recurrences at one location over time.

(I) Spinule lifespan frequency and pie chart of the less than 60 s and 60 s or more spinule subsets (n = 102).

(J) Short-versus long-lived spinule numbers per spine (n = 17). Unpaired Student's t test, p = 0.0196.

(K) Characteristic short-lived spinule shapes (red arrows).

(L) Diverse long-lived spinule shapes (blue arrows).

Data are shown as mean ± SEM. Not significant (NS) ≥ 0.05, *p < 0.05, **p < 0.01, ***p < 0.001, ****p < 0.0001. See also Figure S1.

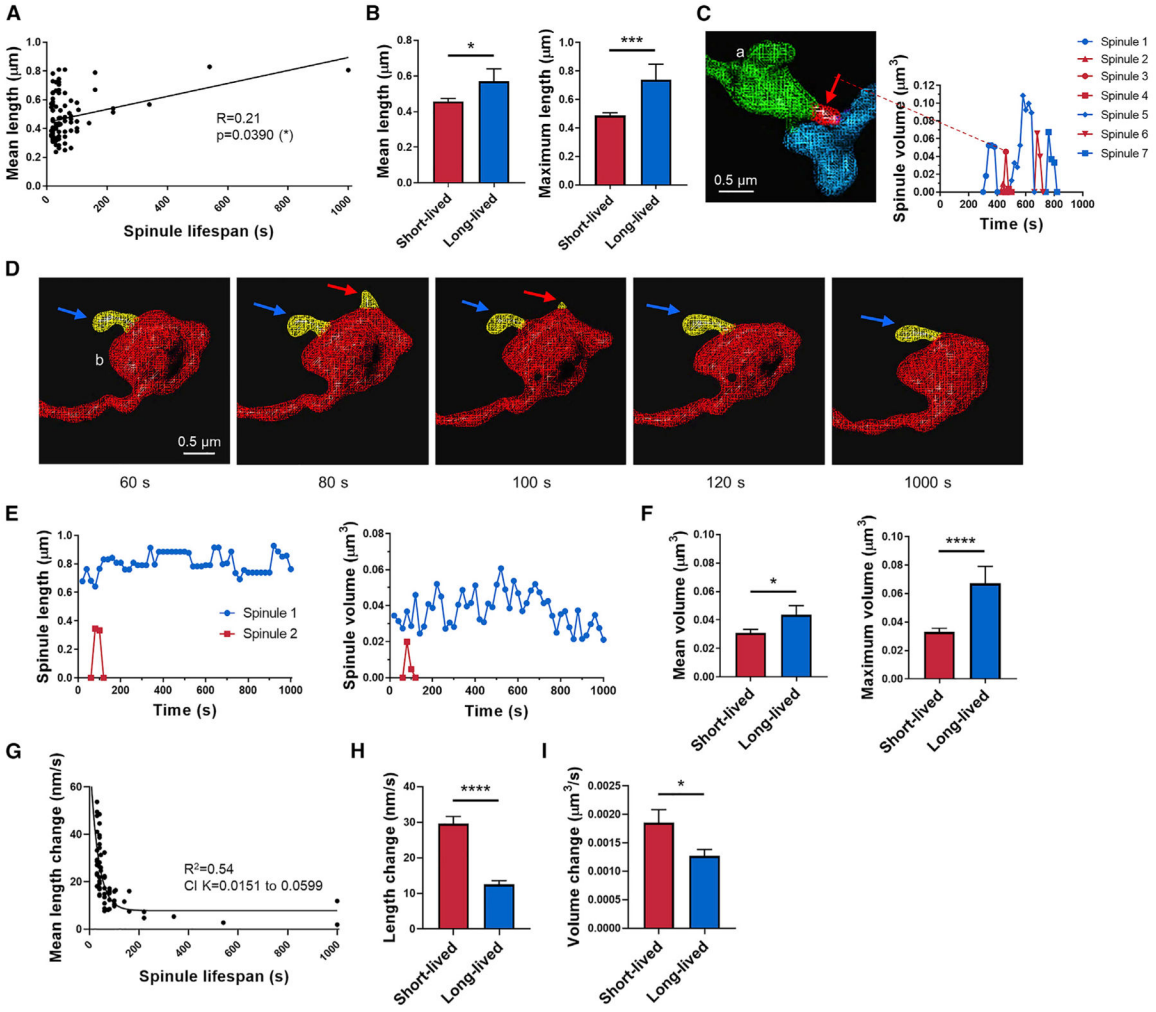

Figure 2. Differential Short- and Long-Lived Spinule Dimensions and Dynamics

(A) Linear regression and Spearman correlation between mean spinule length and lifespan, with a 2.47-μm outlier removed (n = 101).

(B) Mean and maximum length of short-lived (n = 71) versus long-lived spinules (n = 31). Mann-Whitney test, mean p = 0.0436, max. p = 0.0002.

(C) Wireframe 3D model of a single spine (a) and spinule volume (red) and plot of spinule volumes over time.

(D) Montage of a long-lived mushroom spinule (blue arrows) and a short-lived tapered spinule (red arrows).

(E) Length and volume of spinules formed by spine (b).

(F) Mean and maximum volume of short-lived (n = 56) versus long-lived spinules (n = 28). Mann-Whitney test, mean p = 0.0159, maximum p < 0.0001.

(G) Non-linear regression and correlation between mean spinule length change and lifespan, excluding spinules present in a single z stack (n = 62). Confidence interval (CI) K = 0.0151–0.0599.

(H) Mean change in length of spinules grouped by lifespan (n = 62). Unpaired t test, p < 0.0001.

(I) Mean volume change in short-versus long-lived spinules, excluding those in a single z stack (n = 48). Unpaired t test, p = 0.0105.

Data are shown as mean ± SEM. NS ≥ 0.05, *p < 0.05, **p < 0.01, ***p < 0.001, ****p < 0.0001. See also Figure S2.

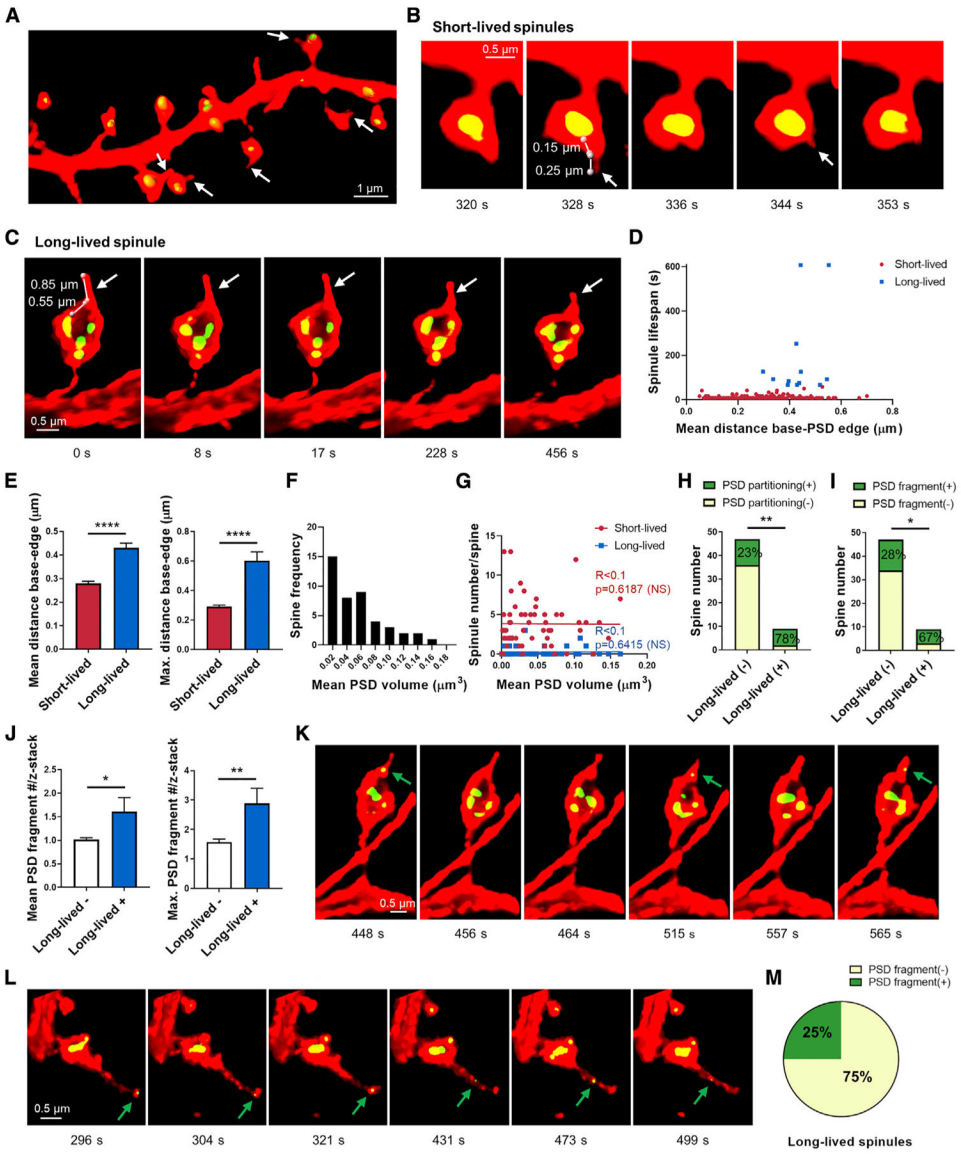

Figure 3. Relationship between Spinule Subsets and PSD Complexity

(A) Enhanced resolution confocal image reconstruction of a dendrite with mushroom spines and their PSD volumes and spinules (arrows) in mRuby- and PSD95-specific GFP-tagged intrabody-expressing neurons.

(B) Montage of recurring short-lived spinules (arrows) originating near a simple PSD edge.

(C) Montage of a long-lived spinule (arrows) originating farther from a complex PSD.

(D) Short- and long-lived spinule lifespans (n = 227) versus mean distance from spinule base to PSD edge.

(E) Mean and maximum distance from base to PSD edge in short-lived (n = 215) versus long-lived spinules (n = 12). Mann-Whitney test, mean $p < 0.0001$, max. $p < 0.0001$.

(F) Binned frequency of mean PSD volume per mushroom spine (n = 56) over time.

(G) Linear regression and Spearman correlation between spinule number per spine and mean PSD volume.

(H) Number of long-lived spinule(−) (n = 47) and spinule(+) (n = 9) spines with PSD partitioning. Fisher's exact test, p = 0.0032.
(I) Number of long-lived spinule(−) or (+) spines displaying fragmented PSDs. Fisher's exact test, p = 0.0491.
(J) Mean and maximum PSD fragment number per z stack in long-lived spinule(−) versus (+) spines. Mann-Whitney test, mean p = 0.0388, max. p = 0.0045.
(K) Montage of a spine with a complex PSD with a small fragment (arrows) trafficking into a long-lived spinule.
(L) Montage of small PSD fragment (arrows) trafficking within a long-lived filopodium spinule. See also Video S2.
(M) Percentage of long-lived spinules (n = 12) displaying a PSD fragment in 1 or more stacks.
Data are represented as mean ± SEM. NS ≥ 0.05, *p < 0.05, **p < 0.01, ***p < 0.001, ****p < 0.0001. See also Figure S3.

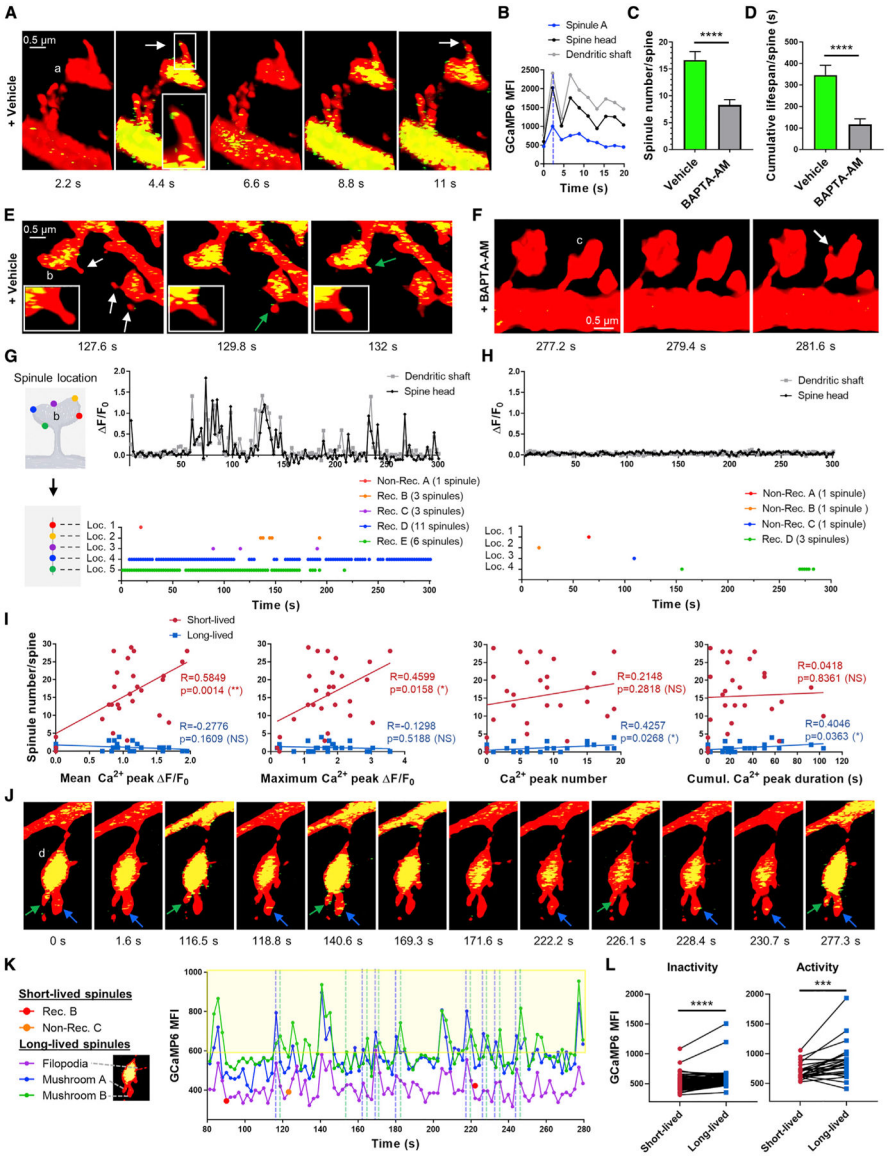

Figure 4. Differential Regulation of Short-Lived and Long-Lived Spinules by Ca^{2+}

(A) Montage of vehicle (DMSO)-treated GCaMP6-expressing spine with Ca^{2+} nanodomains localizing to a long-lived spinule tip (arrows).

(B) Plot of Ca^{2+} transients in the spine head (a), dendritic shaft, and spinule over 20 s.

(C) Comparison of spinule number in vehicle-treated (n = 28) and BAPTA-AM-treated spines (n = 28). Unpaired t test, $p < 0.0001$.

(D) Cumulative spinule lifespan in vehicle-versus BAPTA-AM-treated spines. Mann-Whitney test, $p < 0.0001$.

(E) Vehicle-treated spines with short-lived spinules and long-lived spinules, where Ca^{2+} nanodomains are synchronized to spine head Ca^{2+} peaks (arrows). See also Video S3.

(F) BAPTA-AM-treated spines with dampened Ca^{2+} transients and few dynamic spinules (arrows).

(G) $\Delta F/F_0$ ratio in a vehicle-treated spine head (b) and dendritic shaft with a corresponding temporal recurrent spinule map.
(H) $\Delta F/F_0$ ratio in a BAPTA-AM-treated spine head (c) and dendritic shaft with a corresponding temporal recurrent spinule map.
(I) Linear regression and Pearson correlation of short- and long-lived spinule numbers per spine (n = 27) versus Ca^{2+} peak amplitude, frequency, and duration in control neurons.
(J) Spine montage highlighting enhanced staggered Ca^{2+} transients in two long-lived mushroom spinules. See also Video S4.
(K) Plot of Ca^{2+} transients in short- and long-lived spinules formed by spine (d). The yellow region highlights Ca^{2+} peaks, and dashed lines show staggered Ca^{2+} peaks of two mushroom spinules.
(L) Comparison of GCaMP6 MFI in co-occurring short- versus long-lived spinules during spine head inactivity (n = 75 pairs, $p < 0.0001$) and activity (n = 24 pairs, $p = 0.0007$). Paired Student's t test.
Data are represented as mean ± SEM. NS ≥ 0.05, *p < 0.05, **p < 0.01, ***p < 0.001, ****p < 0.0001. See also Figure S4.

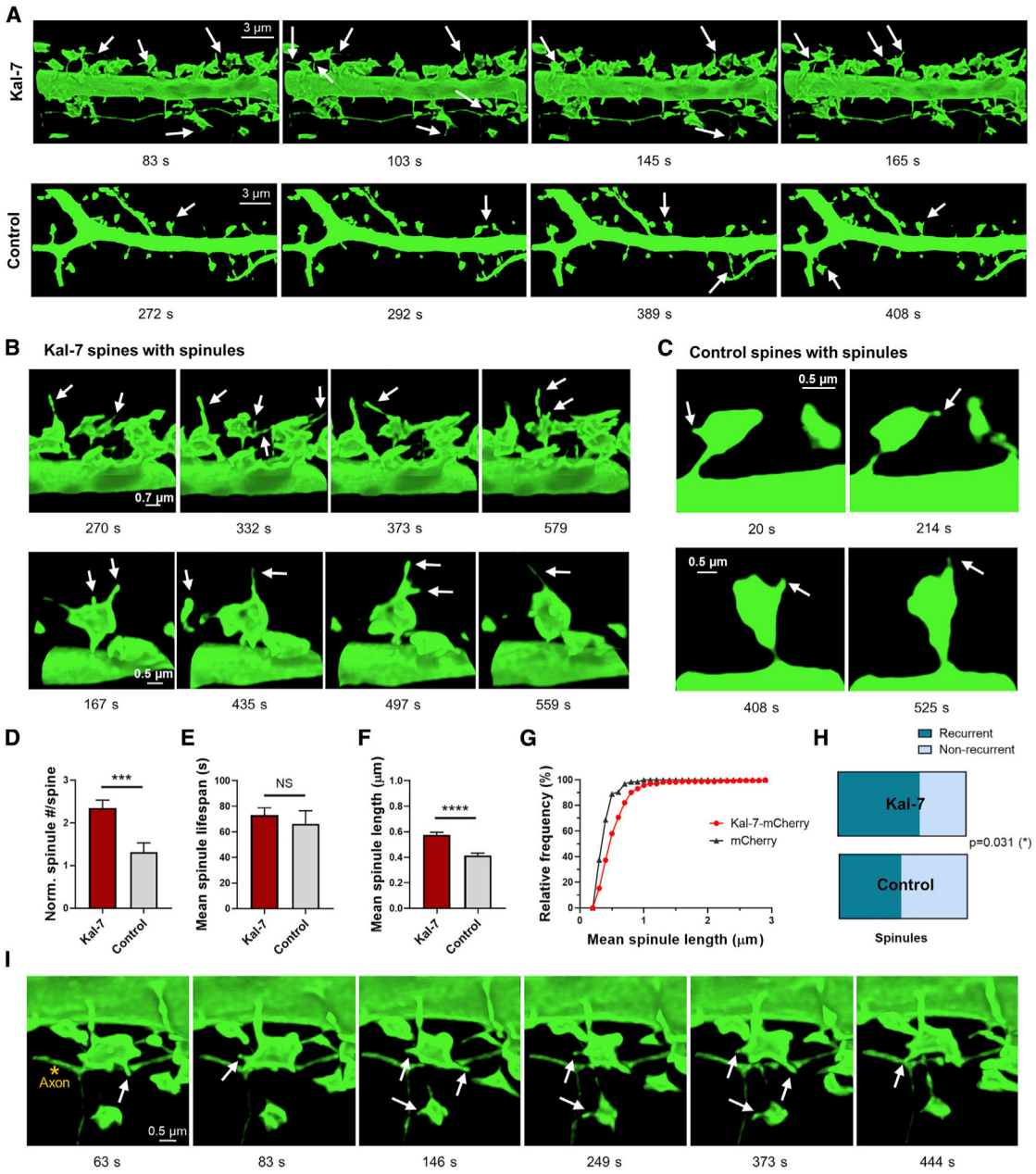

Figure 5. Exogenous Kalirin-7 Expression Enhances Spinule Formation

(A) 3D reconstruction montage of mushroom spine and spinule dynamics (arrows) in kalirin-7 neurons co-expressing pGFP and pLV-Kalirin mCherry versus controls co-expressing pGFP and pLV-mCherry. See also Videos S5 and S6.

(B) Long and variously shaped spinules (arrows) on kalirin-7 spines.

(C) Small dynamic spinules (arrows) on control spines.

(D) Spinule number per spine over 5 min after normalizing to spine volume in kalirin-7 versus control neurons. Mann-Whitney test, p = 0.0003.

(E) Mean spinule lifespan in kalirin-7 (n = 236 spinules) versus control spines (n = 64 spinules). Mann-Whitney test, p = 0.6876.

(F) Mean spinule length comparison. Mann-Whitney test, $p < 0.0001$.
(G) Relative frequency of mean spinule lengths.
(H) Proportion of spinules recurring at one spine head location on kalirin-7 spines (n = 237 spinules) versus controls (n = 64 spinules). Fisher's exact test.
(I) Montage of spinules (arrows) on kalirin-7 spines extending to contact an axon.
Data are represented as mean ± SEM. NS ≥ 0.05, *$p < 0.05$, **$p < 0.01$, ***$p < 0.001$, ****$p < 0.0001$. See also Figure S5.

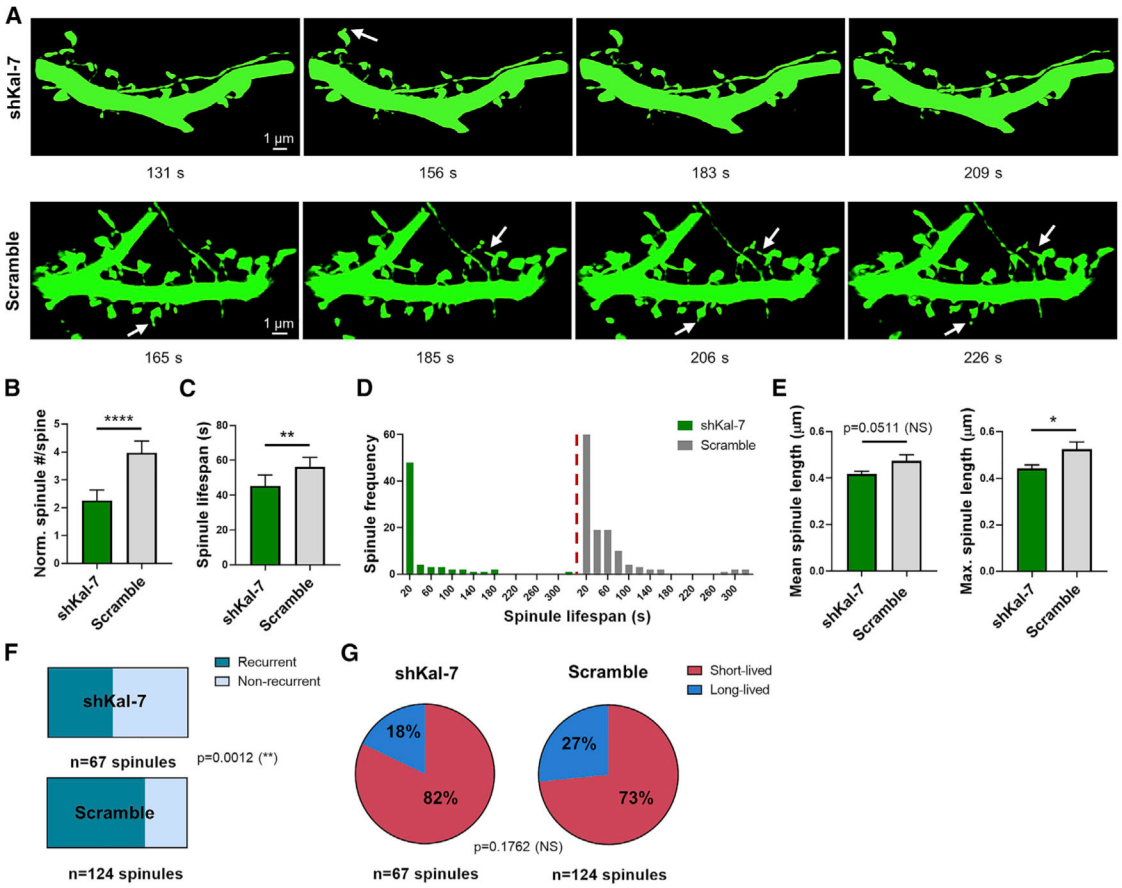

Figure 6. Kalirin-7 Knockdown Inhibits Normal Spinule Formation

(A) Montage of spines and spinules in neurons co-expressing pAAV-shKal-7-GFP and p-mRuby versus pAAV-scramble-GFP and p-mRuby over 300 s.

(B) Spinule number per mushroom spine, normalized to spine volume in shKal-7 (n = 82) and scramble spines (n = 51). Mann-Whitney test, $p < 0.0001$.

(C) Spinule lifespans under shKal-7 (n = 67) versus scramble conditions (n = 124). Mann-Whitney test, $p = 0.0045$.

(D) Frequency of spinule lifespans in shKal-7 versus scramble spines.

(E) Mean and maximum spinule length over time on shKal-7 spines (n = 67 spinules) compared with the scramble (n = 124 spinules). Welch's t test, mean $p = 0.057$, max. $p = 0.0189$.

(F) Proportion of spinules recurring on spines from shKal-7 versus scramble neurons. Chi-square test.

(G) Percentage of short-lived (< 60 s) and long-lived spinules (≥60 s) on shKal-7 versus scramble spines. Chi-square test.

Data are shown as mean ± SEM. NS ≥ 0.05, *$p < 0.05$, **$p < 0.01$, ***$p < 0.001$, ****$p < 0.0001$. See also Figure S6.

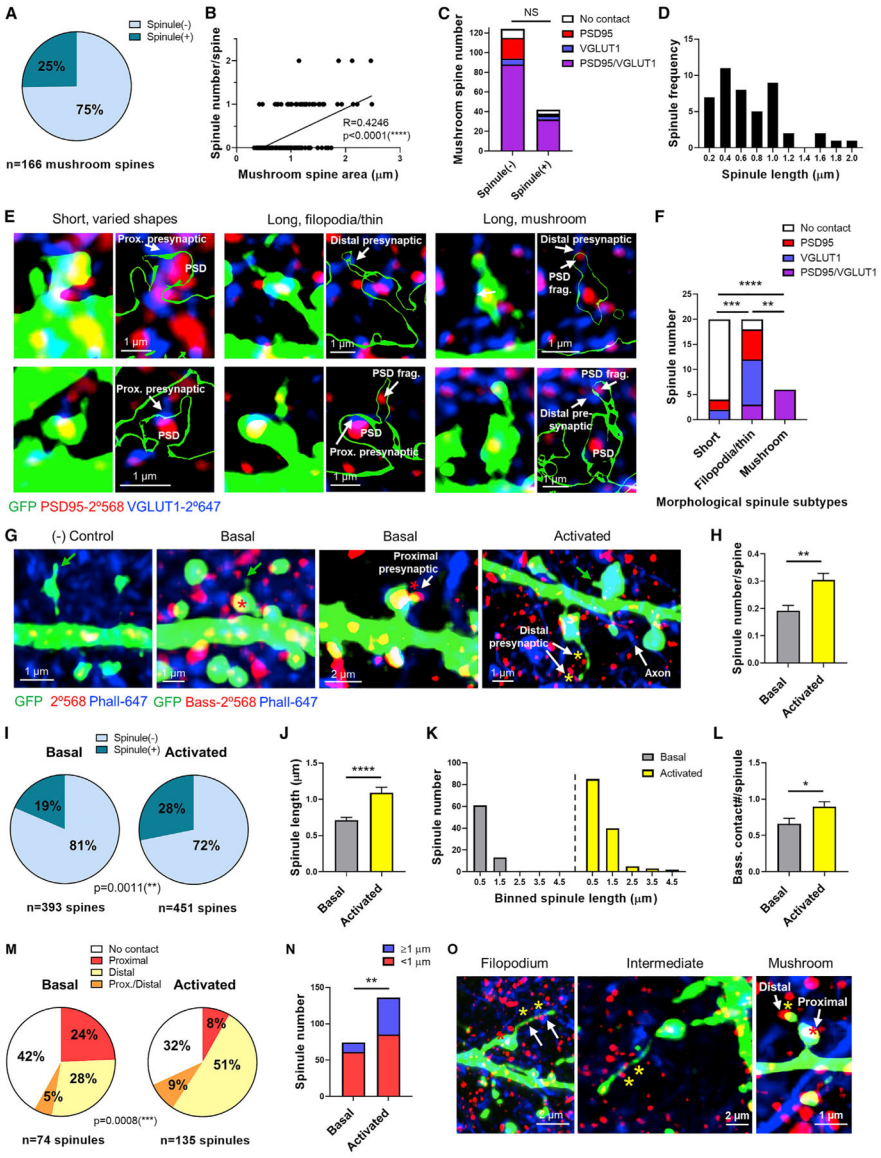

Figure 7. Short Spinules Are Exploratory, whereas Elongated Spinules Contact Distal Synapses and Can Be Induced by Synaptic Activity

(A) Percentage of fixed basal state spinule(−) and (+) mushroom spines immunostained for PSD95 and the presynaptic terminal marker VGLUT1.

(B) Linear regression and Pearson correlation of spinule number per spine versus spine area (n = 166).

(C) Comparison of spinule(−) and (+) mushroom spines colocalizing with PSD95, VGLUT1, PSD95 and VGLUT1, or neither. Chi-square test, p = 0.1852.

(D) Spinule length distribution (n = 46).

(E) Representative 3D reconstructions of short versus long filopodia and thin versus long mushroom spine-shaped spinules and their pre- and postsynaptic contacts.

(F) Short (n = 20), filopodia and thin (n = 20), and mushroom spinules (n = 6) colocalizing with PSD95, VGLUT1, both, or neither. Chi-square test, short versus filopodia and thin p = 0.0001 and versus mushroom p < 0.0001, filopodia and thin versus mushroom p = 0.0021.

(G) Imaris 3D reconstructions of fixed basal versus activated state spinule(+) spines immunostained for bassoon to label spine head-proximal (red asterisk) and -distal presynaptic terminals (yellow asterisk), phalloidin (blue), and spinules (green arrows).
(H) Spinule number per mushroom spine in the basal state (n = 391) versus activated state (n = 449) from maximum projection images. Mann-Whitney test, p = 0.0011.
(I) Spinule(−) and (+) spine percentage in basal versus activated states. Chi-square test.
(J) Spinule lengths in basal (n = 74) and activated states (n = 136). Mann-Whitney test, p < 0.0001.
(K) Frequency distribution of spinule lengths.
(L) Bassoon contact number per spinule. Mann-Whitney test, p = 0.0401.
(M) Spinule percentage contacting spine head-proximal or -distal bassoon, both, or neither. Chi-square test.
(N) Spinule number grouped by length in basal versus activated states. Chi-square test, p = 0.0027.
(O) Imaris reconstructions highlighting spinule shapes (arrows) observed via live imaging. Data are represented as mean ± SEM. NS ≥ 0.05, *p < 0.05, **p < 0.01, ***p < 0.001, ****p < 0.0001. See also Figure S7.

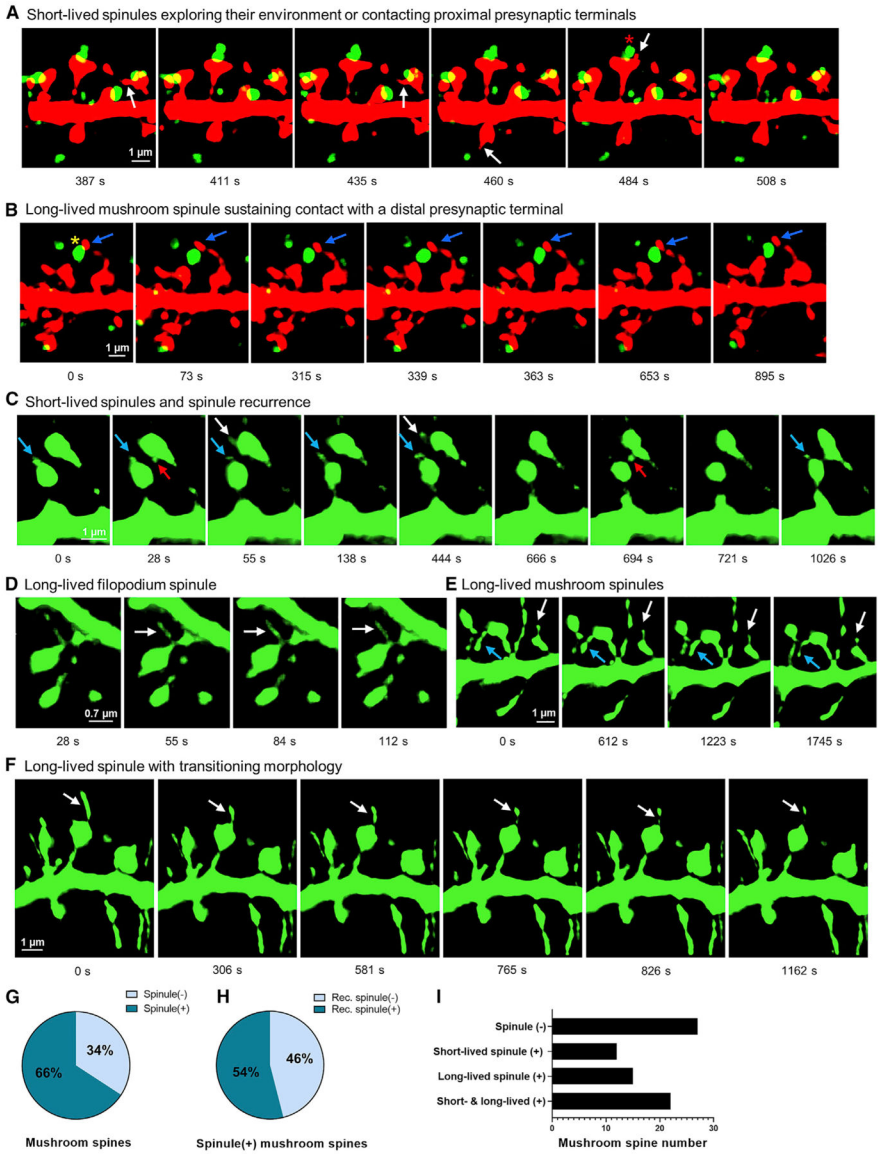

Figure 8. Dynamics of Spinule Subset Interactions with Presynaptic Terminals in Culture and of Spinule Subsets and Recurrence in Live Acute Brain Slices

(A) A 3D reconstruction montage of short-lived spinules (arrows) not contacting FM dye-labeled presynaptic terminals (green) or contacting proximal terminals (red asterisk) in basal-state mRuby-expressing cultured neurons.

(B) Spine montage of dynamic contact between an elongated mushroom spinule (arrows) and large, distal presynaptic terminal (yellow asterisk). See also Video S7.

(C) A 3D montage from live YFP-expressing somatosensory cortical pyramidal neurons in acute brain slices showing recurrent short-lived (red/white arrows) and long-lived spinules (blue arrows). See also Video S8.

(D) Montage of a long-lived filopodium spinule (arrows) existing for 1,200 s or more of imaging.

(E) Long-lived elongated mushroom spinules (arrows) existing for 1,745 s or more. See also Video S9.

(F) Montage of the transition in shape from filopodium to mushroom spinule (arrows).
(G) Spinule(−) and (+) mushroom spine percentage (n = 76) over 1,200 s.
(H) Percentage of spinule(+) mushroom spines (n = 50) displaying recurrent spinules.
(I) Number of spinule(−), short-lived(+), long-lived(+), or short- and long-lived spinule(+) mushroom spines over time.

KEY RESOURCES TABLE

REAGENT or RESOURCE	SOURCE	IDENTIFIER
Antibodies		
Guinea pig polyclonal anti-VGLUTI	Synaptic Systems	Cat#135304; RRID:AB_887878
Mouse monoclonal anti-PSD-95 MAGUK scaffolding protein	NeuroMab	Cat#75–028; RRID:AB_2307331
Guinea pig polyclonal anti-bassoon	Synaptic Systems	Cat#141001; RRID:AB_2290619
Goat polyclonal anti-KALRN	Abcam	Cat#ab52012; RRID:AB_881154
Chemicals, Peptides, and Recombinant Proteins		
Image-iT Fixative Solution	Thermo Fisher Scientific	Cat#FB002
ProLong Gold Antifade Mountant	Thermo Fisher Scientific	Cat#P36934
FM 1–43 Dye	Thermo Fisher Scientific	Cat#T35356
Alexa Fluor 647 Phalloidin	Thermo Fisher Scientific	Cat#A22287
Dynasore	Tocris	Cat#2897
Lipofectamine 2000	Thermo Fisher Scientific	Cat#11668019
Opti-MEM 1X	GIBCO	Cat#31985070
Trypsin, 0.25%	HyClone	Cat#SH3004201
L-amino-phosphonovalerate (APV)	Abcam	Cat#ab120004
BAPTA-AM	Sigma-Aldrich	Cat#A1076
Dimethyl sulfoxide (DMSO)	Sigma-Aldrich	Cat#D2650
Experimental Models: Cell Lines		
HEK293T/17	ATCC	CRL-11268; RRID:SCR_013869
Experimental Models: Organisms/Strains		
Thy1-YFP-H mice	Jackson Laboratories	RRID:IMSR_JAX:003782
C57BL6 mice	Jackson Laboratories	RRID:IMSR_JAX:000664
Oligonucleotides		
Kal-7 shRNA: GCAGTACAATCCTGGCCATGT	Xieetal. (2010)	N/A
Recombinant DNA		
pDsRedExpress2-N1	Clontech	Cat#632537
p-mRuby-N1	Gift from Michael Davidson	Addgene plasmid #54581;http://addgene.org/54581; RRID:Addgene_54581
pCAG_PSD95.FingR-eGFP-CCR5TC	Gift from Don Arnold	Addgene plasmid # 46295;http://addgene.org/46295; RRID:Addgene_46295

REAGENT or RESOURCE	SOURCE	IDENTIFIER
pGP-CMV-GCAMP6s	Gift from Douglas Kim	Addgene plasmid # 40753;http://addgene.org/40753; RRID:Addgene_40753
pGFP	Gift from Stephen Mayfield	Addgene plasmid # 64904;http://addgene.org/64904; RRID:Addgene_64904
pGFP-A-shAAV	Origene	Cat#TR30034
pLV-Kal-7 mCherry [NM_001164268.1]	VectorBuilder	VB181102-1224vxt
pLV-mCherry	VectorBuilder	VB181030-1317wkh
Software and Algorithms		
GraphPad Prism	Graphpad	https://www.graphpad.com/scientific-software/prism/; RRID:SCR_002798
IMARIS	Oxford Instruments	https://imaris.oxinst.com/; RRID:SCR_007370
ImageJ Fiji	NIH	https://imagej.net/; RRID:SCR_002285
NIS Elements	Nikon Instruments	https://www.microscope.healthcare.nikon.com/en_EU/products/software/nis-elements; RRID:SCR 014329